

Online Research @ Cardiff

This is an Open Access document downloaded from ORCA, Cardiff University's institutional repository: <https://orca.cardiff.ac.uk/id/eprint/129090/>

This is the author's version of a work that was submitted to / accepted for publication.

Citation for final published version:

Veres, P., Bhat, P. N., Briggs, M. S., Cleveland, W. H., Hamburg, R., Hui, C. M., Mailyan, B., Preece, R. D., Roberts, O. J., von Kienlin, A., Wilson-Hodge, C. A., Kocovski, D., Arimoto, M., Tak, D., Asano, K., Axelsson, M., Barbiellini, G., Bissaldi, E., Dirirsa, F. Fana, Gill, R., Granot, J., McEnery, J., Omodei, N., Razzaque, S., Piron, F., Racusin, J. L., Thompson, D. J., Campana, S., Bernardini, M. G., Kuin, N. P. M., Siegel, M. H., Cenko, S. B., O'Brien, P., Capalbi, M., Dai, A., De Pasquale, M., Gropp, J., Klingler, N., Osborne, J. P., Perri, M., Starling, R. L. C., Tagliaferri, G., Tohuvavohu, A., Ursi, A., Tavani, M., Cardillo, M., Casentini, C., Piano, G., Evangelista, Y., Verrecchia, F., Pittori, C., Lucarelli, F., Bulgarelli, A., Parmiggiani, N., Anderson, G. E., Anderson, J. P., Bernardi, G., Bolmer, J., Caballero-García, M. D., Carrasco, I. M., Castellón, A., Segura, N. Castro, Castro-Tirado, A. J., Cherukuri, S. V., Cockeram, A. M., D'Avanzo, P., Di Dato, A., Diretse, R., Fender, R. P., Fernández-García, E., Fynbo, J. P. U., Fruchter, A. S., Greiner, J., Gromadzki, M., Heintz, K. E., Heywood, I., van der Horst, A. J., Hu, Y.-D., Inserra, C. ORCID: <https://orcid.org/0000-0002-3968-4409>, Izzo, L., Jaiswal, V., Jakobsson, P., Japelj, J., Kankare, E., Kann, D. A., Kouveliotou, C., Klose, S., Levan, A. J., Li, X. Y., Lotti, S., Maguire, K., Malesani, D. B., Manulis, I., Marongiu, M., Martin, S., Melandri, A., Michalowski, M. J., Miller-Jones, J. C. A., Misra, K., Moin, A., Mooley, K. P., Nasri, S., Nicholl, M., Noschese, A., Novara, G., Pandey, S. B., Peretti, E., del Pulgar, C. J. Pérez, Pérez-Torres, M. A., Perley, D. A., Piro, L., Ragosta, E., Resmi, L., Ricci, R., Rossi, A., Sánchez-Ramírez, R., Selsing, J., Schulze, S., Smartt, S. J., Smith, I. A., Sokolov, V. V., Stevens, J., Tanvir, N. R., Thöne, C. C., Tiengo, A., Tremou, E., Troja, E., de Ugarte Postigo, A., Valeev, A. E., Vergani, S. D., Wieringa, M., Woudt, P. A., Xu, D., Yaron, O., Young, D. R. and MAGIC Collaboration 2019. Observation of inverse Compton emission from a long γ ray burst. *Nature* 575 (7783), pp. 459-463. 10.1038/s41586-019-1754-6 file

Publishers page: <http://dx.doi.org/10.1038/s41586-019-1754-6>
<<http://dx.doi.org/10.1038/s41586-019-1754-6>>

Please note:

Changes made as a result of publishing processes such as copy-editing, proof correction and page numbers may not be reflected in this version. For the definitive version of this publication, please refer to the published source. You

information services
gwasanaethau gwybodaeth



are advised to consult the publisher's version if you wish to cite this paper.

This version is being made available in accordance with publisher policies.

See

<http://orca.cf.ac.uk/policies.html> for usage policies. Copyright and moral rights
for publications made available in ORCA are retained by the copyright
holders.

Observation of Inverse Compton emission from a gamma ray burst

V. A. Acciari¹, S. Ansoldi^{2,3}, L. A. Antonelli⁴, A. Arbet Engels⁵, D. Baack⁶, A. Babić⁷,
B. Banerjee⁸, U. Barres de Almeida⁹, J. A. Barrio¹⁰, J. Becerra González¹, W. Bednarek¹¹,
L. Bellizzi¹², E. Bernardini^{13,14}, A. Berti¹⁵, J. Besenrieder¹⁷, W. Bhattacharyya¹³, C. Bigongiari⁴,
A. Biland⁵, O. Blanch¹⁶, G. Bonnoli¹², Ž. Bošnjak⁷, G. Busetto¹⁴, R. Carosi²⁰, G. Ceribella¹⁷,
Y. Chai¹⁷, A. Chilingaryan¹⁸, S. Cikota⁷, S. M. Colak¹⁶, U. Colin¹⁷, E. Colombo¹, J. L. Contreras¹⁰,
J. Cortina¹⁹, S. Covino⁴, V. D’Elia⁴, P. Da Vela²⁰, F. Dazzi⁴, A. De Angelis¹⁴, B. De Lotto²,
M. Delfino^{16,21}, J. Delgado^{16,21}, D. Depaoli¹⁵, F. Di Pierro¹⁵, L. Di Venere¹⁵, E. Do Souto
Espíñeira¹⁶, D. Dominis Prester⁷, A. Donini², D. Dorner²², M. Doro¹⁴, D. Elsaesser⁶, V. Fallah
Ramazani²³, A. Fattorini⁶, G. Ferrara⁴, D. Fidalgo¹⁰, L. Foffano¹⁴, M. V. Fonseca¹⁰, L. Font²⁴,
C. Fruck¹⁷, S. Fukami³, R. J. García López¹, M. Garczarczyk¹³, S. Gasparyan¹⁸, M. Gaug²⁴,
N. Giglietto¹⁵, F. Giordano¹⁵, N. Godinović⁷, D. Green¹⁷, D. Guberman¹⁶, D. Hadasch³,
A. Hahn¹⁷, J. Herrera¹, J. Hoang¹⁰, D. Hrupec⁷, M. Hütten¹⁷, T. Inada³, S. Inoue³, K. Ishio¹⁷,
Y. Iwamura³, L. Jouvin¹⁶, D. Kerszberg¹⁶, H. Kubo³, J. Kushida³, A. Lamastra⁴, D. Lelas⁷,
F. Leone⁴, E. Lindfors²³, S. Lombardi⁴, F. Longo^{2,25,26}, M. López¹⁰, R. López-Coto¹⁴,
A. López-Oramas¹, S. Loporchio¹⁵, B. Machado de Oliveira Fraga⁹, C. Maggio²⁴, P. Majumdar⁸,
M. Makariev²⁷, M. Mallamaci¹⁴, G. Maneva²⁷, M. Manganaro⁷, K. Mannheim²², L. Maraschi⁴,
M. Mariotti¹⁴, M. Martínez¹⁶, D. Mazin^{3,17}, S. Mićanović⁷, D. Miceli², M. Minev²⁷,
J. M. Miranda¹², R. Mirzoyan¹⁷, E. Molina²⁸, A. Moralejo¹⁶, D. Morcuende¹⁰, V. Moreno²⁴,
E. Moretti¹⁶, P. Munar-Adrover²⁴, V. Neustroev²³, C. Nigro¹³, K. Nilsson²³, D. Ninci¹⁶,

K. Nishijima³, K. Noda³, L. Nogués¹⁶, S. Nozaki³, S. Paiano¹⁴, M. Palatiello², D. Paneque¹⁷,
R. Paoletti¹², J. M. Paredes²⁸, P. Peñil¹⁰, M. Peresano², M. Persic², P. G. Prada Moroni²⁰,
E. Prandini¹⁴, I. Puljak⁷, W. Rhode⁶, M. Ribó²⁸, J. Rico¹⁶, C. Righi⁴, A. Rugliancich²⁰, L. Saha¹⁰,
N. Sahakyan¹⁸, T. Saito³, S. Sakurai³, K. Satalecka¹³, K. Schmidt⁶, T. Schweizer¹⁷, J. Sitarek¹¹,
I. Šnidarić⁷, D. Sobczynska¹¹, A. Somero¹, A. Stamerra⁴, D. Strom¹⁷, M. Strzys¹⁷, Y. Suda¹⁷,
T. Surić⁷, M. Takahashi³, F. Tavecchio⁴, P. Temnikov²⁷, T. Terzić⁷, M. Teshima^{3,17},
N. Torres-Albà²⁸, L. Tosti¹⁵, V. Vagelli¹⁵, J. van Scherpenberg¹⁷, G. Vanzo¹, M. Vazquez Acosta¹,
C. F. Vigorito¹⁵, V. Vitale¹⁵, I. Vovk¹⁷, M. Will¹⁷, D. Zarić⁷

L. Nava^{4,25,29},

P. Veres³⁰, P. N. Bhat³⁰, M. S. Briggs^{30,31}, W. H. Cleveland³², R. Hamburg^{30,31}, C. M. Hui³³,
B. Mailyan³⁰, R. D. Preece^{30,31}, O. Roberts³², A. von Kienlin³⁴, C. A. Wilson-Hodge³³,
D. Kocevski³³, M. Arimoto³⁵, D. Tak^{36,37}, K. Asano³⁸, M. Axelsson^{39,40}, G. Barbiellini²⁵,
E. Bissaldi^{41,42}, R. Gill⁴³, J. Granot⁴³, J. McEnery^{36,37}, N. Omodei⁴⁴, S. Razzaque⁴⁵, F. Piron⁴⁶,
J. L. Racusin³⁷, D. J. Thompson³⁷,

S. Campana⁴⁷, M. G. Bernardini⁴⁷, N. P. M. Kuin⁴⁸, M. H. Siegel⁴⁹, S. Bradley Cenko^{37,50}, P.
OBrien⁵¹, M. Capalbi⁵², A. D'Alò⁵², M. De Pasquale⁵³, J. Gropp⁴⁹, N. Klingler⁴⁹, J. P. Osborne⁵¹,
M. Perri^{54,55}, R. Starling⁵¹, G. Tagliaferri^{47,52}, A. Tohuvavohu⁴⁹,

A. Ursi⁵⁶, M. Tavani^{56,57,58}, M. Cardillo⁵⁶, C. Casentini⁵⁶, G. Piano⁵⁶, Y. Evangelista⁵⁶,
F. Verrecchia^{54,55}, C. Pittori^{54,55}, F. Lucarelli^{54,55}, A. Bulgarelli⁵⁵, N. Parmiggiani⁵⁵,

G. E. Anderson⁵⁹, J. P. Anderson⁶⁰, G. Bernardi^{61,62,63}, J. Bolmer³⁴, M. D. Caballero-García⁶⁴,
 I. M. Carrasco⁶⁵, A. Castellón⁶⁶, N. Castro Segura⁶⁷, A. J. Castro-Tirado^{68,69}, S. V. Cherukuri⁷⁰,
 A. M. Cockeram⁷¹, P. D'Avanzo⁴⁷, A. Di Dato^{72,73}, R. Diretse⁷⁴, R.P. Fender⁷⁵,
 E. Fernández-García⁶⁹, J. P. U. Fynbo^{76,77}, A.S. Fruchter⁷⁸ J. Greiner³⁴, M. Gromadzki⁷⁹, K.E.
 Heintz⁸⁰ I. Heywood^{62,75}, A.J. van der Horst^{81,82}, Y.-D. Hu^{69,83}, C. Inserra⁸⁴, L. Izzo^{69,85},
 V. Jaiswal⁷⁰, P. Jakobsson⁸⁰, J. Japelj⁸⁶, E. Kankare⁸⁷, D. A. Kann⁶⁹, C. Kouveliotou^{81,82},
 S. Klose⁸⁸, A. J. Levan⁸⁹, X. Y. Li^{90,91}, S. Lotti⁵⁶, K. Maguire⁹², D. B. Malesani^{76,77,85,93},
 I. Manulis⁹⁴, M. Marongiu^{95,96}, S. Martin^{60,97}, A. Melandri⁴⁷, M. Michałowski⁹⁸,
 J.C.A. Miller-Jones⁵⁹, K. Misra^{99,100}, A. Moin¹⁰¹, K.P. Mooley^{102,103}, S. Nasri¹⁰¹,
 M. Nicholl^{104,105}, A. Noschese⁷², G. Novara^{106,107}, S. B. Pandey⁹⁹, E. Peretti^{58,108}, C. J. Pérez del
 Pulgar⁶⁸, M.A. Pérez-Torres^{69,109}, D. A. Perley⁷¹, L. Piro⁵⁶, F. Ragosta^{73,110,111}, L. Resmi⁷⁰,
 R. Ricci⁶¹ A. Rossi¹¹², R. Sánchez-Ramírez⁵⁶, J. Selsing⁷⁷ S. Schulze¹¹³, S. J. Smartt¹¹⁴,
 I. A. Smith¹¹⁵, V. V. Sokolov¹¹⁶, J. Stevens¹¹⁷, N. R. Tanvir⁵¹, C. C. Thóne⁶⁹, A. Tiengo^{106,107,118},
 E. Tremou¹¹⁹, E. Troja^{37,120}, A. de Ugarte Postigo^{69,85}, A. F. Valeev¹¹⁶, S. D. Vergani¹²¹,
 M. Wieringa¹²², P.A. Woudt⁷⁴, D. Xu¹²³, O. Yaron⁹⁴, D. R. Young¹¹⁴

¹*Inst. de Astrofísica de Canarias, E-38200 La Laguna, and Universidad de La Laguna, Dpto.
 Astrofísica, E-38206 La Laguna, Tenerife, Spain*

²*Università di Udine, and INFN Trieste, I-33100 Udine, Italy*

³*Japanese MAGIC Consortium: ICRR, The University of Tokyo, 277-8582 Chiba, Japan; Depart-
 ment of Physics, Kyoto University, 606-8502 Kyoto, Japan; Tokai University, 259-1292 Kanagawa,
 Japan; RIKEN, 351-0198 Saitama, Japan*

- ⁴*National Institute for Astrophysics (INAF), I-00136 Rome, Italy*
- ⁵*ETH Zurich, CH-8093 Zurich, Switzerland*
- ⁶*Technische Universität Dortmund, 44221 Dortmund, Germany*
- ⁷*Croatian Consortium: University of Rijeka, Department of Physics, 51000 Rijeka; University of Split - FESB, 21000 Split; University of Zagreb - FER, 10000 Zagreb; University of Osijek, 31000 Osijek; Rudjer Boskovic Institute, 10000 Zagreb, Croatia*
- ⁸*Saha Institute of Nuclear Physics, HBNI, 1/AF Bidhannagar, Salt Lake, Sector-1, Kolkata 700064, India*
- ⁹*Centro Brasileiro de Pesquisas Físicas (CBPF), 22290-180 URCA, Rio de Janeiro (RJ), Brasil*
- ¹⁰*Unidad de Partículas y Cosmología (UPARCOS), Universidad Complutense, E-28040 Madrid, Spain*
- ¹¹*University of Lodz, Faculty of Physics and Applied Informatics, Department of Astrophysics, 90-236 Lodz, Poland*
- ¹²*Università di Siena and INFN Pisa, I-53100 Siena, Italy*
- ¹³*Deutsches Elektronen-Synchrotron (DESY), 15738 Zeuthen, Germany*
- ¹⁴*Università di Padova and INFN, I-35131 Padova, Italy*
- ¹⁵*Istituto Nazionale Fisica Nucleare (INFN), 00044 Frascati (Roma) Italy*
- ¹⁶*Institut de Física d'Altes Energies (IFAE), The Barcelona Institute of Science and Technology (BIST), E-08193 Bellaterra (Barcelona), Spain*
- ¹⁷*Max-Planck-Institut für Physik, 80805 München, Germany*
- ¹⁸*The Armenian Consortium: ICRANet-Armenia at NAS RA, A. Alikhanyan National Laboratory*

83 ¹⁹*Centro de Investigaciones Energéticas, Medioambientales y Tecnológicas, E-28040 Madrid, Spain*

84 ²⁰*Università di Pisa, and INFN Pisa, I-56126 Pisa, Italy*

85 ²¹*also at Port d'Informació Científica (PIC) E-08193 Bellaterra (Barcelona) Spain*

86 ²²*Universität Würzburg, 97074 Würzburg, Germany*

87 ²³*Finnish MAGIC Consortium: Finnish Centre of Astronomy with ESO (FINCA), University of*
88 *Turku, FI-20014 Turku, Finland; Astronomy Research Unit, University of Oulu, F90014 Oulu,*
89 *Finland*

90 ²⁴*Departament de Física, and CERES-IEEC, Universitat Autònoma de Barcelona, E-08193 Bel-*
91 *laterra, Spain*

92 ²⁵*Istituto Nazionale di Fisica Nucleare, Sezione di Trieste, 34149 Trieste, Italy*

93 ²⁶*also at Dipartimento di Fisica, Università di Trieste, 34127 Trieste, Italy*

94 ²⁷*Inst. for Nucl. Research and Nucl. Energy, Bulgarian Academy of Sciences, BG-1784 Sofia,*
95 *Bulgaria*

96 ²⁸*Universitat de Barcelona, ICCUB, IEEC-UB, E-08028 Barcelona, Spain*

97 ²⁹*Institute for Fundamental Physics of the Universe (IFPU), 34151 Trieste, Italy*

98 ³⁰*Center for Space Plasma and Aeronomic Research, University of Alabama in Huntsville, 320*
99 *Sparkman Drive, Huntsville, AL 35899, USA*

100 ³¹*Space Science Department, University of Alabama in Huntsville, 320 Sparkman Drive,*
101 *Huntsville, AL 35899, USA*

102 ³²*Science and Technology Institute, Universities Space Research Association, Huntsville, AL*
103 *35805, USA*

- 104 ³³*Astrophysics Office, ST12, NASA/Marshall Space Flight Center, Huntsville, AL 35812, USA*
- 105 ³⁴*Max-Planck Institut für extraterrestrische Physik, Giessenbachstraße 1, 85748 Garching, Ger-*
106 *many*
- 107 ³⁵*Faculty of Mathematics and Physics, Institute of Science and Engineering, Kanazawa University,*
108 *Kakuma, Kanazawa, Ishikawa 920-1192*
- 109 ³⁶*Department of Physics, University of Maryland, College Park, MD 20742-4111, USA*
- 110 ³⁷*Astrophysics Science Division, NASA Goddard Space Flight Center, 8800 Greenbelt Rd, Green-*
111 *belt, MD 20771, USA*
- 112 ³⁸*Institute for Cosmic-Ray Research, University of Tokyo, 5-1-5 Kashiwanoha, Kashiwa, Chiba,*
113 *277-8582, Japan*
- 114 ³⁹*Department of Physics, Stockholm University, AlbaNova, SE-106 91 Stockholm, Sweden*
- 115 ⁴⁰*Department of Physics, KTH Royal Institute of Technology, AlbaNova, SE-106 91 Stockholm,*
116 *Sweden*
- 117 ⁴¹*Dipartimento di Fisica “M. Merlin” dell’Università e del Politecnico di Bari, 70126 Bari, Italy*
- 118 ⁴²*Istituto Nazionale di Fisica Nucleare, Sezione di Bari, 70126 Bari, Italy*
- 119 ⁴³*Department of Natural Sciences, Open University of Israel, 1 University Road, POB 808,*
120 *Ra’anana 43537, Israel*
- 121 ⁴⁴*W. W. Hansen Experimental Physics Laboratory, Kavli Institute for Particle Astrophysics and*
122 *Cosmology, Department of Physics and SLAC National Accelerator Laboratory, Stanford Univer-*
123 *sity, Stanford, CA 94305, USA*
- 124 ⁴⁵*Department of Physics, University of Johannesburg, PO Box 524, Auckland Park 2006, South*

Africa

⁴⁶Laboratoire Univers et Particules de Montpellier, Université Montpellier, CNRS/IN2P3, F-34095

Montpellier, France

⁴⁷INAF - Astronomical Observatory of Brera, I-23807 Merate (LC), Italy

⁴⁸Mullard Space Science Laboratory, University College London, Holmbury St. Mary, Dorking,

RH5 6NT, United Kingdom

⁴⁹Department of Astronomy and Astrophysics, Pennsylvania State University. 525 Davey Laboratory, University Park, PA 16802, USA

⁵⁰Joint Space-Science Institute, University of Maryland, College Park, Maryland 20742, USA

⁵¹Department of Physics and Astronomy, University of Leicester, University Road, Leicester LE1 7RH, UK

⁵²INAF Istituto di Astrofisica Spaziale e Fisica Cosmica di Palermo, via Ugo La Malfa 153, I-90146 Palermo, Italia

⁵³Department of Astronomy and Space Sciences, Istanbul University, Fatih, 34119, Istanbul, Turkey

⁵⁴INAF-Osservatorio Astronomico di Roma, Via Frascati 33, I-00078 Monteporzio Catone, Italy

⁵⁵Space Science Data Center (SSDC), Agenzia Spaziale Italiana (ASI), via del Politecnico s.n.c., I-00133, Roma, Italy

⁵⁶INAF-IAPS, via del Fosso del Cavaliere 100, I-00133 Roma, Italy

⁵⁷Univ. "Tor Vergata", Via della Ricerca Scientifica 1, I-00133 Roma, Italy

⁵⁸Gran Sasso Science Institute, viale Francesco Crispi 7, I-67100 L'Aquila, Italy

- ⁵⁹*International Centre for Radio Astronomy Research, Curtin University, GPO Box U1987, Perth,*
WA 6845, Australia
- ⁶⁰*European Southern Observatory, Alonso de Còrdova, 3107, Vitacura, Santiago 763-0355, Chile*
- ⁶¹*INAF-Istituto di Radioastronomia, via Gobetti 101, I-40129, Bologna, Italy*
- ⁶²*Department of Physics and Electronics, Rhodes University, PO Box 94, Grahamstown, 6140,*
South Africa
- ⁶³*South African Radio Astronomy Observatory, Black River Park, 2 Fir Street, Observatory, Cape*
Town, 7925, South Africa
- ⁶⁴*Astronomical Institute of the Academy of Sciences, Boční II 1401, CZ-14100 Praha 4, Czech*
Republic
- ⁶⁵*Departamento de Física Aplicada, Facultad de Ciencias, Universidad de Málaga, Bulevar Louis*
Pasteur 31, E-29071 Málaga, Spain
- ⁶⁶*Departamento de Álgebra, Geometría y Topología, Facultad de Ciencias, Bulevar Louis Pasteur*
31, Universidad de Málaga, E-29071 Málaga, Spain
- ⁶⁷*Physics and Astronomy Department, University of Southampton, Southampton, UK*
- ⁶⁸*Unidad Asociada Departamento de Ingeniería de Sistemas y Automática, E.T.S. de Ingenieros*
Industriales, Universidad de Málaga, Arquitecto Francisco Peñalosa 6, E-29071 Málaga, Spain
- ⁶⁹*Instituto de Astrofísica de Andalucía (IAA-CSIC), Glorieta de la Astronomía, s/n, E-18008,*
Granada, Spain
- ⁷⁰*Indian Institute of Space Science & Technology, Trivandrum 695547, India*
- ⁷¹*Astrophysics Research Institute, Liverpool John Moores University, 146 Brownlow Hill, Liver-*

167 *pool L3 5RF, UK*

168 ⁷²*Osservatorio Astronomico 'S. Di Giacomo' - AstroCampania, I-80051, Agerola (NA), Italy*

169 ⁷³*INAF - Astronomical Observatory of Naples, I-23807 Naples (NA), Italy*

170 ⁷⁴*Inter-University Institute for Data-Intensive Astronomy, Department of Astronomy, University*
171 *of Cape Town, Private Bag X3, Rondebosch 7701, South Africa*

172 ⁷⁵*Astrophysics, Department of Physics, University of Oxford, Keble Road, Oxford OX1 3RH, UK*

173 ⁷⁶*Cosmic Dawn Center (DAWN)*

174 ⁷⁷*Niels Bohr Institute, Copenhagen University, Vibenshuset, Lyngbyvej 2, DK-2100, Copenhagen*

175 ⁷⁸*Space Telescope Science Institute, 3700 San Martin Drive, Baltimore, MD 21218, USA*

176 ⁷⁹*Warsaw University Astronomical Observatory, Al. Ujazdowskie 4, PL-00- 478 Warszawa,*
177 *Poland*

178 ⁸⁰*Centre for Astrophysics and Cosmology, Science Institute, University of Iceland, Dunhagi 5, 107*
179 *Reykjavík, Iceland*

180 ⁸¹*Department of Physics, The George Washington University, 725 21st Street NW, Washington,*
181 *DC 20052, USA*

182 ⁸²*Astronomy, Physics, and Statistics Institute of Sciences (APSIS), The George Washington Uni-*
183 *versity, Washington, DC 20052, USA*

184 ⁸³*Universidad de Granada, Facultad de Ciencias Campus Fuentenueva S/N CP 18071 Granada,*
185 *Spain*

186 ⁸⁴*School of Physics & Astronomy, Cardiff University, Queens Buildings, The Parade, 25 Cardiff,*
187 *CF24 3AA, UK*

- 188 ⁸⁵*DARK, Niels Bohr Institute, University of Copenhagen, Lyngbyvej 2, DK-2100 Copenhagen Ø,*
189 *Denmark*
- 190 ⁸⁶*Anton Pannekoek Institute for Astronomy, University of Amsterdam, Science Park 904, 1098*
191 *XH Amsterdam, The Netherlands*
- 192 ⁸⁷*Tuorla Observatory, Department of Physics and Astronomy, University of Turku, 20014 Turku,*
193 *Finland*
- 194 ⁸⁸*Thüringer Landessternwarte Tautenburg, Sternwarte 5, 07778 Tautenburg, Germany*
- 195 ⁸⁹*Department of Astrophysics/IMAPP, Radboud University Nijmegen, The Netherlands*
- 196 ⁹⁰*Instituto de Hortofruticultura Subtropical y Mediterránea La Mayora (IHSM/UMA-CSIC), Al-*
197 *garrobo Costa s/n, E-29750 Málaga, Spain*
- 198 ⁹¹*Nanjing Institute for Astronomical Optics and Technology, National Observatories, Chinese*
199 *Academy of Sciences, 188 Bancang St, Xuanwu Qu, Nanjing Shi, Jiangsu Sheng, China*
- 200 ⁹²*School of Physics, Trinity College Dublin, Dublin 2, Ireland*
- 201 ⁹³*DTU Space, National Space Institute, Technical University of Denmark, Elektrovej 327, 2800*
202 *Kongens Lyngby, Denmark*
- 203 ⁹⁴*Benozio Center for Astrophysics, Weizmann Institute of Science, 76100 Rehovot, Israel*
- 204 ⁹⁵*Department of Physics and Earth Science, University of Ferrara, via Saragat 1, I-44122, Ferrara,*
205 *Italy*
- 206 ⁹⁶*International Center for Relativistic Astrophysics Network (ICRANet), Piazzale della Repub-*
207 *blica 10, I-65122, Pescara, Italy*
- 208 ⁹⁷*Joint ALMA Observatory, Alonso de Còrdova, 3107, Vitacura, Santiago 763-0355, Chile*

⁹⁸*Astronomical Observatory Institute, Faculty of Physics, Adam Mickiewicz University,
 ul. Słoneczna 36, 60-286 Poznań, Poland*

⁹⁹*Aryabhata Research Institute of Observational Sciences, Manora Peak, Nainital 263 001, India*

¹⁰⁰*Department of Physics, University of California, 1 Shields Ave, Davis, CA 95616-5270, USA*

¹⁰¹*Physics Department, United Arab Emirates University, P.O. Box 15551, Al-Ain, United Arab
 Emirates*

¹⁰²*National Radio Astronomy Observatory, 1003 Lopezville Road, Socorro, NM 87801, USA*

¹⁰³*Caltech, 1200 California Blvd., Pasadena, CA 91106, USA*

¹⁰⁴*Institute for Astronomy, University of Edinburgh, Royal Observatory, Blackford Hill, EH9 3HJ,
 UK*

¹⁰⁵*Birmingham Institute for Gravitational Wave Astronomy and School of Physics and Astronomy,
 University of Birmingham, Birmingham B15 2TT, UK*

¹⁰⁶*Scuola Universitaria Superiore IUSS Pavia, Piazza della Vittoria 15, 27100 Pavia, Italy*

¹⁰⁷*INAF - IASF Milano, Via E. Bassini 15, 20133 Milano, Italy*

¹⁰⁸*INFN / Laboratori Nazionali del Gran Sasso, Via G. Acitelli 22, 67100, Assergi (AQ), Italy*

¹⁰⁹*Depto. de Física Teórica, Universidad de Zaragoza, E-50019, Zaragoza, Spain*

¹¹⁰*Dipartimento di Scienze Fisiche, Universit degli studi di Napoli Federico II, Via Cinthia, Edifi-
 cio N, 80126 Napoli, Italy*

¹¹¹*INFN, Sezione di Napoli, Complesso Universitario di Monte S. Angelo, Via Cinthia, Edificio
 N, 80126 Napoli, Italy*

¹¹²*INAF - Osservatorio di Astrofisica e Scienza dello Spazio, via Piero Gobetti 93/3, 40129*

230 *Bologna, Italy*

231 ¹¹³*Department of Particle Physics and Astrophysics, Weizmann Institute of Science, Rehovot*
232 *76100, Israel*

233 ¹¹⁴*Astrophysics Research Centre, School of Mathematics and Physics, Queen's University Belfast,*
234 *Belfast BT7 1NN, UK*

235 ¹¹⁵*Department of Physics and Astronomy, Rice University, 6100 South Main, MS-108, Houston,*
236 *TX 77251-1892, USA*

237 ¹¹⁶*Special Astrophysical Observatory, Nizhniy Arkhyz, Zelenchukskiy region, Karachai-*
238 *Cherkessian Republic, 369167, Russia*

239 ¹¹⁷*CSIRO Australia Telescope National Facility, Paul Wild Observatory, Narrabri NSW 2390, Aus-*
240 *tralia*

241 ¹¹⁸*Istituto Nazionale di Fisica Nucleare, Sezione di Pavia, Via Bassi 6, 27100 Pavia, Italy*

242 ¹¹⁹*AIM, CEA, CNRS, Université Paris Diderot, Sorbonne Paris Cité, Université Paris-Saclay, F-*
243 *91191 Gif-sur-Yvette, France*

244 ¹²⁰*Department of Astronomy, University of Maryland, College Park, MD 20742-4111, USA*

245 ¹²¹*GEPI, Observatoire de Paris, PSL University, CNRS, 5 Place Jules Janssen, 92190 Meudon,*
246 *France*

247 ¹²²*Australia Telescope National Facility, CSIRO Astronomy and Space Science, PO Box 76, Ep-*
248 *ping, NSW 1710, Australia*

249 ¹²³*CAS Key Laboratory of Space Astronomy and Technology, National Astronomical Observato-*
250 *ries, Chinese Academy of Sciences, Beijing 100012, China*

Long-duration gamma-ray bursts (GRBs) originate from ultra-relativistic jets launched from the collapsing cores of dying massive stars. They are characterised by an initial phase of bright and highly variable radiation in the keV-MeV band that is likely produced within the jet and lasts from milliseconds to minutes, known as the prompt emission^{1,2}. Subsequently, the interaction of the jet with the external medium generates external shock waves, responsible for the afterglow emission, which lasts from days to months, and occurs over a broad energy range, from the radio to the GeV bands¹⁻⁶. The afterglow emission is generally well explained as synchrotron radiation by electrons accelerated at the external shock⁷⁻⁹. Recently, an intense, long-lasting emission between 0.2 and 1 TeV was observed from the GRB 190114C¹⁰. Here we present the results of our multi-frequency observational campaign of GRB 190114C, and study the evolution in time of the GRB emission across 17 orders of magnitude in energy, from 5×10^{-6} up to 10^{12} eV. We find that the broadband spectral energy distribution is double-peaked, with the TeV emission constituting a distinct spectral component that has power comparable to the synchrotron component. This component is associated with the afterglow, and is satisfactorily explained by inverse Compton upscattering of synchrotron photons by high-energy electrons.

We find that the conditions required to account for the observed TeV component are not atypical, supporting the possibility that inverse Compton emission is commonly produced in GRBs.

On 14 January 2019, following an alert from the Neil Gehrels Swift Observatory (hereafter *Swift*) and the *Fermi* satellite, the Major Atmospheric Gamma Imaging Cherenkov (MAGIC)

272 **telescopes** observed and detected radiation up to at least 1 TeV from GRB 190114C. Before the
 273 MAGIC detection, GRB emission has only been reported at much lower energies, $\lesssim 100$ GeV, first
 274 by *CGRO*/EGRET in a handful of cases, and more recently by *AGILE*/GRID and *Fermi*/LAT (see
 275 ¹¹ for a recent review).

276 Detection of TeV radiation opens a new window in the electromagnetic spectrum for the
 277 study of GRBs¹⁰. Its announcement¹² triggered an extensive campaign of follow-up observations.
 278 Owing to the relatively low redshift $z = 0.4245 \pm 0.0005$ (see Methods) of the GRB (corresponding
 279 to a luminosity distance of ~ 2.3 Gpc) a comprehensive set of multi-wavelength data could be
 280 collected. We present observations gathered from instruments onboard six satellites and 15 ground
 281 telescopes (radio, submm and NIR/optical/UV and very high energy gamma-rays; see Methods)
 282 for the first ten days after the burst. The frequency range covered by these observations spans more
 283 than 17 orders of magnitude, from 1 to $\sim 2 \times 10^{17}$ GHz, the most extensive to date for a GRB. The
 284 light curves of GRB 190114C at different frequencies are shown in Fig. 1.

285 The prompt emission of GRB 190114C was simultaneously observed by several space mis-
 286 sions (see Methods), covering the spectral range from 8 keV to ~ 100 GeV. The prompt light curve
 287 shows a complex temporal structure, with several emission peaks (Methods; Extended Data Fig. 1),
 288 with total duration ~ 25 s (see dashed line in Fig. 1) and total radiated energy $E_{\gamma, \text{iso}} = (2.5 \pm 0.1)$
 289 $\times 10^{53}$ ergs (isotropic equivalent, in the energy range $1 - 10^4$ keV¹³). During the time of inter-burst
 290 quiescence at $t \sim [5 - 15]$ seconds and after the end of the last prompt pulse at $t \gtrsim 25$ s, the flux
 291 decays smoothly, following a power law in time $F \propto t^\alpha$, with $\alpha_{10-1000\text{keV}} = -1.10 \pm 0.01$ ¹³. The

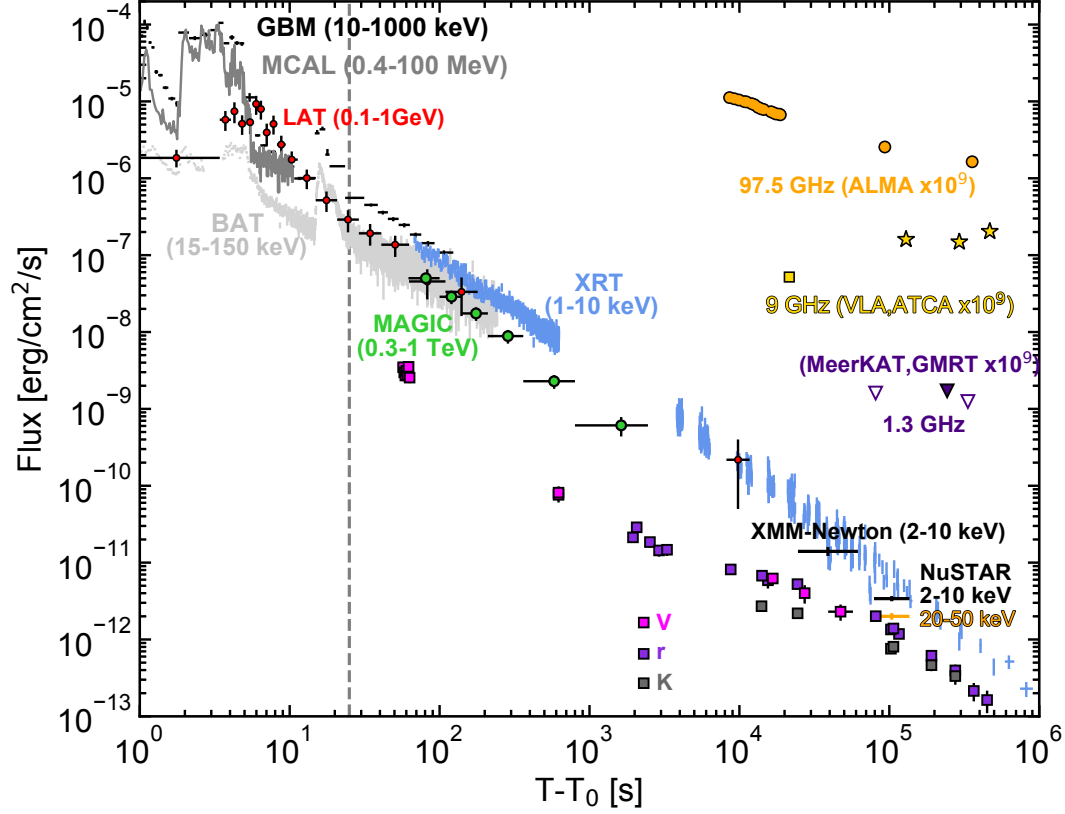


Figure 1: **Multi-wavelength light curves of GRB 190114C.** Energy flux at different wavelengths, from radio to gamma-rays, versus time since the BAT trigger time $T_0 = 20:57:03.19$ UT on 14 January 2019. The light curve for the energy range 0.3-1 TeV (green circles) is compared with light curves at lower frequencies. Those for VLA (yellow square), ATCA (yellow stars), ALMA (orange circles), GMRT (purple filled triangle), and MeerKAT (purple empty triangles) have been multiplied by 10^9 for clarity. The vertical dashed line marks approximately the end of the prompt emission phase, identified with the end of the last flaring episode. For the data points, vertical bars show the $1-\sigma$ errors on the flux, while horizontal bars represent the duration of the observation.

temporal and spectral characteristics of this smoothly varying component support an interpretation in terms of afterglow synchrotron radiation, making this one of the few clear cases of afterglow emission detected in the band $10 - 10^4$ keV during the prompt emission phase. The onset of the afterglow component is then estimated to occur around $t \sim 5 - 10$ s^{13,14}, implying an initial bulk Lorentz factor between 300 and 700 (Methods).

After about one minute from the start of the prompt emission, two additional high-energy telescopes began observations: MAGIC and *Swift*/XRT. The XRT and MAGIC light curves (1-10 keV, blue data points in Fig. 1, and 0.3-1 TeV, green data points, respectively) decay with time as a power law, and display the following decay rates: $\alpha_X \sim -1.36 \pm 0.02$ and $\alpha_{\text{TeV}} \sim -1.51 \pm 0.04$. The 0.3-1 TeV light curve shown in Fig. 1 was obtained after correcting for attenuation by the extragalactic background light (EBL)¹⁰. The TeV-band emission is observable until ~ 40 minutes, which is much longer than the nominal duration of the prompt emission phase. The NIR-optical light curves (square symbols) show a more complex behaviour. Initially, a fast decay is seen, where the emission is most likely dominated by the reverse shock component¹⁵. This is followed by a shallower decay, and subsequently a faster decay at $t \gtrsim 10^5$ s. The latter behaviour might indicate that the characteristic synchrotron frequency ν_m is crossing the optical band (Extended Data Fig. 6), which is not atypical, but usually occurs at earlier times. The relatively late time at which the break appears in GRB 190114C would then imply a very large value of ν_m , placing it in the X-ray band at $\sim 10^2$ s. The millimeter light curves (orange symbols) also show an initial fast decay where the emission is dominated by the reverse shock, followed by emission at late times with nearly constant flux (Extended Data Fig. 3).

The spectral energy distributions (SEDs) of the radiation detected by MAGIC are shown in Fig. 2, where the whole duration of the emission detected by MAGIC is divided into five time intervals. For the first two time intervals, observations in the GeV and X-ray bands are also available. During the first time interval (68-110 s, blue data points and blue confidence regions), *Swift*/XRT-BAT and *Fermi*/GBM data show that the afterglow synchrotron component is peaking in the X-ray band. At higher energies, up to $\lesssim 1$ GeV, the SED is a decreasing function of energy, as supported by the *Fermi*/LAT flux between 0.1 and 0.4 GeV (see Methods). On the other hand, at even higher energies, the MAGIC flux above 0.2 TeV implies a spectral hardening. This evidence is independent of the EBL model adopted to correct for the attenuation (Methods). This demonstrates that the newly discovered TeV radiation is not a simple extension of the known afterglow synchrotron emission, but rather a separate spectral component that has never been clearly seen before.

The extended duration and the smooth, power-law temporal decay of the radiation detected by MAGIC (see green data points in Fig. 1) suggest an intimate connection between the TeV emission and the broadband afterglow emission. The most natural candidate is synchrotron self-Compton (SSC) radiation in the external forward shock: the same population of relativistic electrons responsible for the afterglow synchrotron emission Compton upscatters the synchrotron photons, leading to a second spectral component that peaks at higher energies. TeV afterglow emission can also be produced by hadronic processes such as synchrotron radiation by protons accelerated to ultra-high energies in the forward shock^{16–18}. However, due to their typically low efficiency of radiation⁶, reproducing the luminous TeV emission as observed here by such processes would imply unrealistically large power in accelerated protons¹⁰. TeV photons can also be produced via

the SSC mechanism in internal shock synchrotron models of the prompt emission. However, numerical modeling (Methods) shows that prompt SSC radiation can account at most for a limited fraction ($\lesssim 20\%$) of the observed TeV flux, and only at early times ($t \lesssim 100$ s). Henceforth, we focus on the SSC process in the afterglow.

SSC emission has been predicted for GRB afterglows^{9,11,17,19–26}. However, its quantitative significance was uncertain, as the SSC luminosity and spectral properties depend strongly on the poorly constrained physical conditions in the emission region (e.g., the magnetic field strength). The detection of the TeV component in GRB 190114C and the availability of **multi-band** observations offer the opportunity to investigate the relevant physics at a deeper level. SSC radiation might have been already detected in very bright GRBs, such as GRB 130427A. Photons with energies 10–100 GeV, as those detected in GRB 130427A are challenging to explain by the synchrotron processes, suggesting a different origin^{27–29}.

We model the full data set (from radio band to TeV energies, for the first week after the explosion) as synchrotron plus SSC radiation, within the framework of the theory of afterglow emission from external forward shocks. The detailed modeling of the broadband emission and its evolution with time is presented in Section Methods. We discuss here the implications for the emission at $t < 2400$ s and energies above > 1 keV.

The soft spectra in the 0.2–1 TeV energy range (photon index $\Gamma_{\text{TeV}} < -2$; see Extended Data Table 1) constrain the peak of the SSC component to be below this energy range. The relatively small ratio between the spectral peak energies of the SSC ($E_{\text{p}}^{\text{SSC}} \lesssim 200$ GeV) and synchrotron

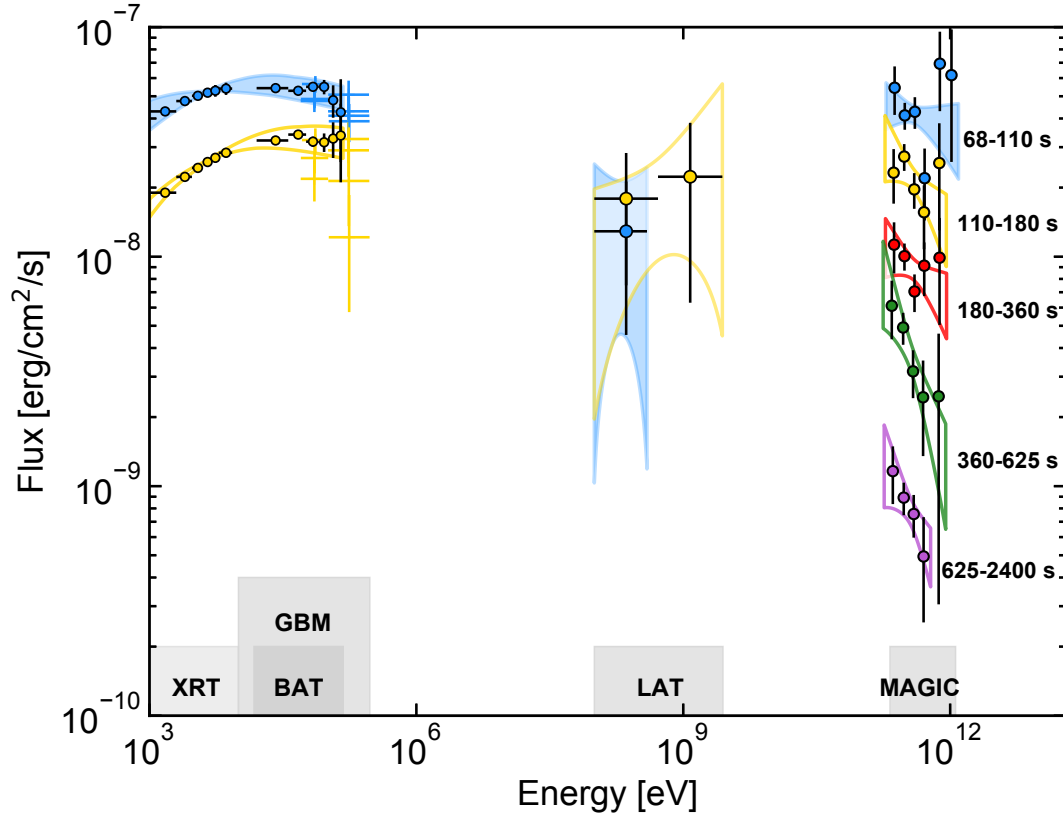


Figure 2: **Multi-band spectra in the time interval 68-2400 s.** Five time intervals are considered: 68-110 s (blue), 110-180 s (yellow), 180-360 s (red), 360-625 s (green), 625-2400 s (purple). MAGIC data points have been corrected for attenuation caused by the **extragalactic background light**. Data from other instruments are shown for the first two time-intervals: *Swift*/XRT, *Swift*/BAT, *Fermi*/GBM, and *Fermi*/LAT. For each time interval, LAT contour regions are shown limiting the energy range to the range where photons are detected. MAGIC and LAT contour regions are drawn from the $1\text{-}\sigma$ error of their best-fit power law functions. For *Swift* data, the regions show the 90% confidence contours for the joint fit XRT-BAT obtained fitting to the data a smoothly broken power law. Filled regions are used for the first time interval (68-110 s, blue color).

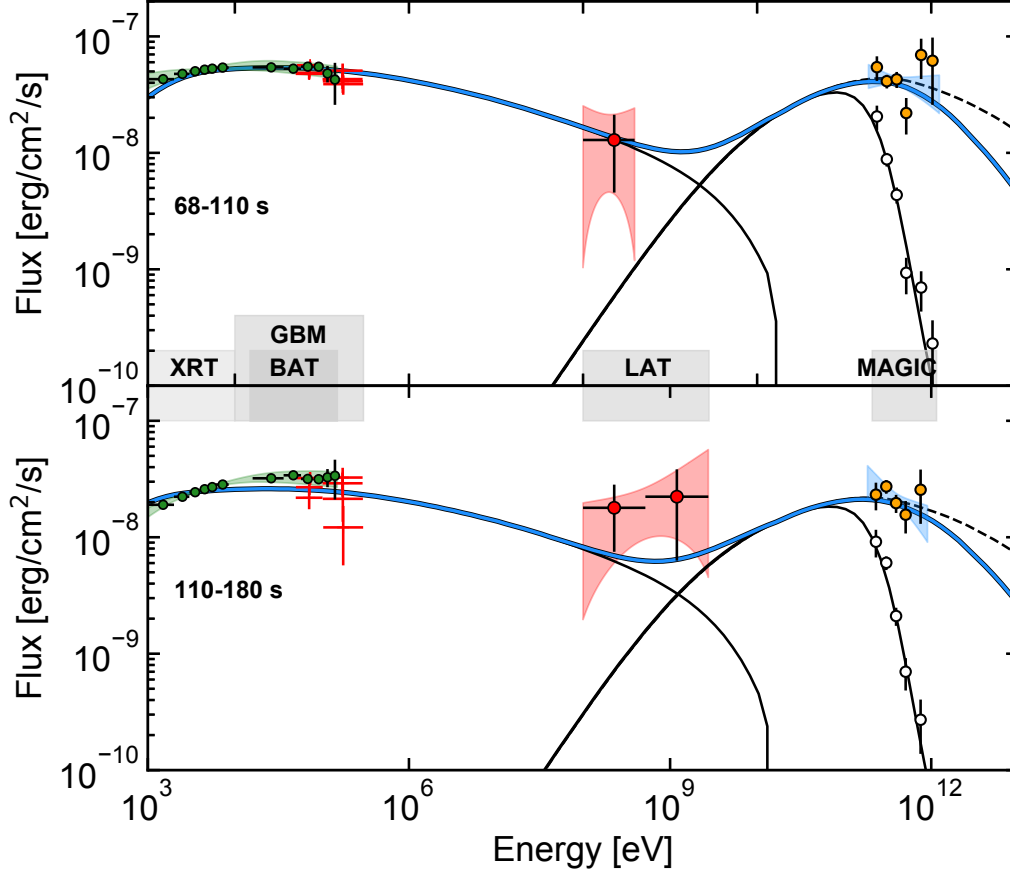


Figure 3: **Modeling of the broadband spectra in the time intervals 68-110 s and 110-180 s.**

Thick blue curve: modeling of the **multi-band** data in the synchrotron and SSC afterglow scenario.

Thin solid lines: synchrotron and SSC (observed spectrum) components; dashed lines: SSC if

internal γ - γ opacity is neglected. The adopted parameters are: $s = 0$, $\epsilon_e = 0.07$, $\epsilon_B = 8 \times 10^{-5}$,

$p = 2.6$, $n_0 = 0.5$, and $E_k = 8 \times 10^{53}$ erg, see the Text. Empty circles show the observed MAGIC

spectrum, i.e. not corrected by attenuation caused by the **extragalactic background light**. Contour

regions and data points as in Fig. 2.

354 ($E_p^{\text{syn}} \sim 10 \text{ keV}$) components implies a relatively low value for the Lorentz factor of the electrons
 355 ($\gamma \sim 2 \times 10^3$). This value is hard to reconcile with the observation of the synchrotron peak at $\gtrsim \text{keV}$
 356 energies. In order to explain the soft spectrum detected by MAGIC, it is necessary to invoke **the**
 357 **Klein-Nishina** (KN) regime scattering for the electrons radiating at the spectral peak as well
 358 as internal γ - γ absorption³⁰. While both effects tend to become less important with time, the
 359 spectral index in the 0.2-1 TeV band remains constant in time (or possibly evolves to softer values;
 360 Extended Data Table 1). This implies that the SSC peak energy is moving to lower energies and
 361 crossing the MAGIC energy band. The energy at which attenuation by internal pair production
 362 becomes important indicates that the bulk Lorentz factor is ~ 140 -160 at 100 s.

363 An example of the theoretical modeling in this scenario is shown in Fig. 3 (blue solid curve,
 364 see Methods for details). The dashed line shows the SSC spectrum when internal absorption is
 365 neglected. The thin solid line shows the model spectrum including EBL attenuation, in comparison
 366 to **the MAGIC observations** (empty circles).

367 We find that acceptable models of the broadband SED can be obtained if the conditions at
 368 the source are the following. The initial kinetic energy of the blastwave is $E_k \gtrsim 3 \times 10^{53} \text{ erg}$
 369 (isotropic-equivalent). The electrons swept up from the external medium are efficiently injected
 370 into the acceleration process, and carry a fraction $\epsilon_e \sim 0.05 - 0.15$ of the energy dissipated at
 371 the shock. The acceleration mechanism produces an electron population characterized by a non-
 372 thermal energy distribution, described by a power law with index $p \sim 2.4 - 2.6$, injection Lorentz
 373 factor $\gamma_m = (0.8 - 2) \times 10^4$ and maximum Lorentz factor $\gamma_{\text{max}} \sim 10^8$ (at $\sim 100 \text{ s}$). The magnetic

374 field behind the shock conveys a fraction $\epsilon_B \sim (0.05 - 1) \times 10^{-3}$ of the dissipated energy. At
 375 $t \sim 100$ s, corresponding to $R \sim (8 - 20) \times 10^{16}$ cm, the density of the external medium is
 376 $n \sim 0.5 - 5 \text{ cm}^{-3}$, and the magnetic field strength is $B \sim 0.5 - 5$ Gauss. The latter implies that
 377 the magnetic field was efficiently amplified from values of a few μGauss that are typical of the
 378 unshocked ambient medium, due to plasma instabilities or other mechanisms⁶. Not surprisingly,
 379 we find that $\epsilon_e \gg \epsilon_B$, that is a necessary condition for the efficient production of SSC radiation^{17,19}.

380 The blastwave energy inferred from the modeling is comparable to the amount of energy
 381 released in the form of radiation during the prompt phase. The prompt emission mechanism must
 382 then have dissipated and radiated no more than half of the initial jet energy, leaving the other half
 383 available for the afterglow phase. The modeling of the **multi-band** data also allows us to infer how
 384 the total energy is shared between the synchrotron and the SSC components. The resultant power
 385 in the two components are comparable. We estimate that the energy in the synchrotron and SSC
 386 component are $\sim 1.5 \times 10^{52}$ erg and $\sim 6.0 \times 10^{51}$ erg respectively in the time interval 68-110 s, and
 387 $\sim 1.3 \times 10^{52}$ erg and $\sim 5.4 \times 10^{51}$ erg respectively in the time interval 110-180 s. Thus, previous
 388 studies of GRBs may have been missing a significant fraction of the energy emitted during the
 389 afterglow phase that is essential to its understanding.

390 Finally, we note that the values of the afterglow parameters inferred from the modeling fall
 391 within the range of values typically inferred from broadband (radio-to-GeV) studies of GRB af-
 392 terglow emission. This points to the possibility that SSC emission in GRBs may be a relatively
 393 common process that does not require special conditions to be produced with power similar to

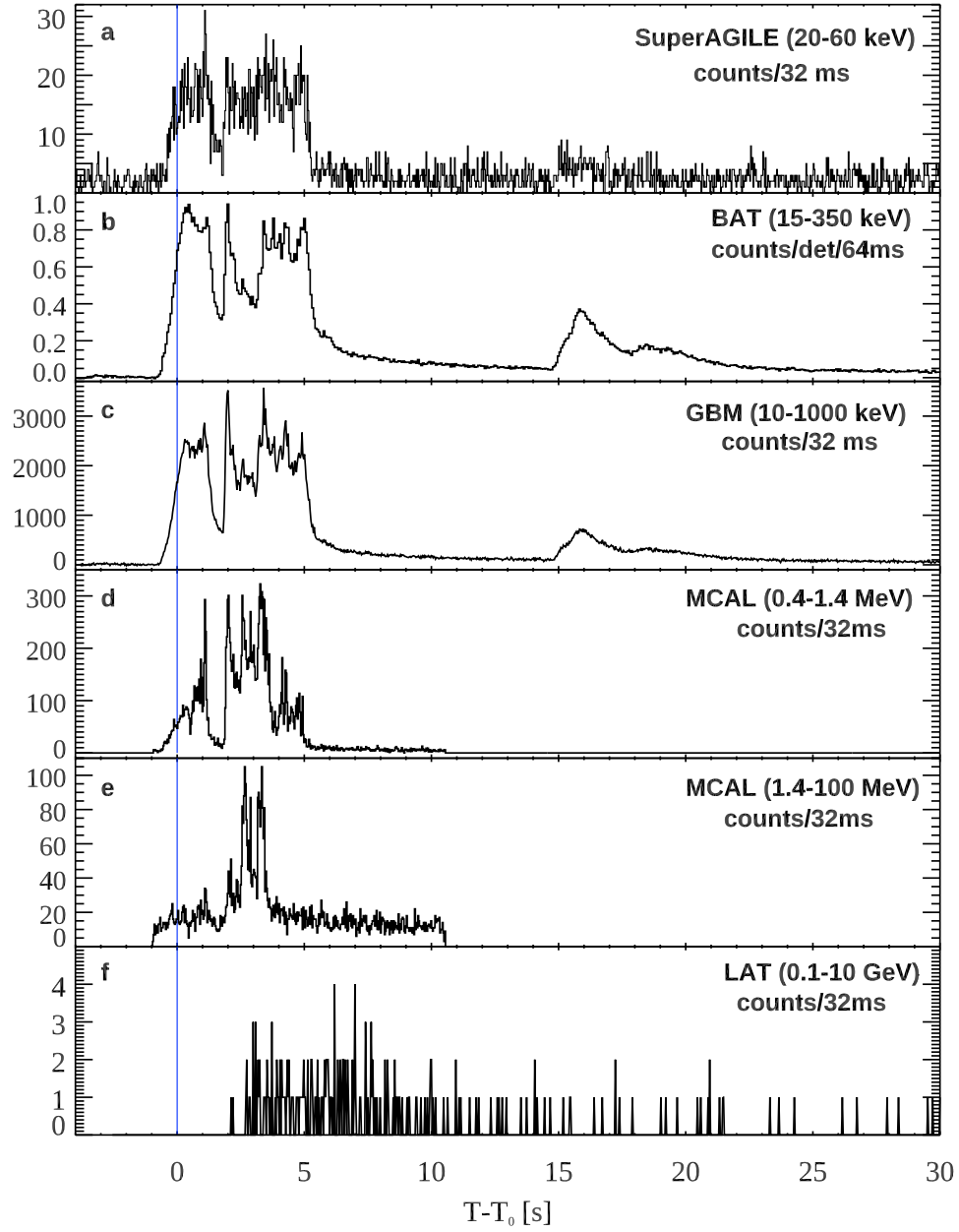
394 synchrotron radiation.

395 The SSC component may then be detectable at TeV energies in other relatively energetic
396 GRBs, as long as the redshift is low enough to avoid severe attenuation by the EBL. This also
397 provides support to earlier indications for SSC emission at GeV energies ^{27–29}.

Methods

Prompt emission observations On 14 January 2019, the prompt emission from GRB 190114C triggered several space instruments, including *Fermi*/GBM³¹, *Fermi*/LAT³², *Swift*/BAT³³, Super-AGILE³⁴, AGILE/MCAL³⁴, KONUS/Wind³⁵, INTEGRAL/SPI-ACS³⁶, and *Insight*/HXMT³⁷. The prompt emission light curves from AGILE, *Fermi*, and *Swift* are shown in Fig. 1 and in Extended Data Fig. 1, where the trigger time T_0 (here and elsewhere) refers to the BAT trigger time (20:57:03.19 UT). The prompt emission lasts approximately for 25 s, where the last flaring emission episode ends. Nominally, the T_{90} , i.e. the time interval during which a fraction between 5% and 95% of the total emission is observed, is much longer (> 100 s, depending on the instrument¹³), but is clearly contaminated by the afterglow component (Fig. 1) and does not provide a good measure of the actual duration of the prompt emission. A more detailed study of the prompt emission phase is reported in¹³.

AGILE (The Astrorivelatore Gamma ad Immagini LEggero³⁸) could observe GRB 190114C until T_0+330 s, before it became occulted by the Earth. GRB 190114C triggered the Mini-CALorimeter (MCAL) from $T_0-0.95$ s to $T_0+10.95$ s. The MCAL light flux curve in Fig. 1 has been produced using two different spectral models. From $T_0-0.95$ s to $T_0+1.8$ s, the spectrum is fitted by a power law with photon index $\Gamma_{\text{ph}} = -1.97^{+0.47}_{-0.70}$ ($dN/dE \propto E^{\Gamma_{\text{ph}}}$). From $T_0+1.8$ s to $T_0+5.5$ s the best fit model is a broken power law with $\Gamma_{\text{ph},1} = -1.87^{+0.54}_{-0.19}$, $\Gamma_{\text{ph},2} = -2.63^{+0.07}_{-0.07}$, and break energy $E_b = 756^{+137}_{-159}$ keV. The total fluence in the 0.4–100 MeV energy range is $F = 1.75 \times 10^{-4}$ erg cm⁻². The Super-AGILE detector also detected the burst, but the large off-axis angle prevented any X-ray imaging of the burst, as well as spectral analysis. Panels **a**, **d**, and **e**



Extended Data Figure 1: **Prompt emission light curves for different detectors.** The different panels show light curves for: **a**, SuperAGILE (20-60 keV); **b**, *Swift*/BAT (15-150 keV); **c**, *Fermi*/GBM (10-1000 keV); **d**, *AGILE*/MCAL (0.4-1.4 MeV); **e**, *AGILE*/MCAL (1.4-100 MeV); **f**, *Fermi*/LAT (0.1-10 GeV). The light curve of *AGILE*/MCAL is split into two bands to show the energy dependence of the first peak. Error bars show the $1-\sigma$ statistical errors.

in Extended Data Fig. 1 show the GRB 190114C light curves acquired by the Super-AGILE detector (20 – 60 keV) and by the MCAL detector in the low- (0.4 – 1.4 MeV) and high-energy (1.4 – 100 MeV) bands.

Fermi/GBM At the time of the MAGIC observations there are indications that some of the detectors are partially blocked by structure on the *Fermi* Spacecraft that is not modeled in the GBM detectors’ response. This affects the low-energy part of the spectrum³⁹. For this reason, out of caution we elected to exclude the energy channels below 50 keV. The spectra detected by the *Fermi*-Gamma-ray Burst Monitor (GBM)⁴⁰ during the T_0+68 s to T_0+110 s and T_0+110 s to T_0+180 s intervals are best described by a power law model with photon index $\Gamma_{\text{ph}} = -2.10 \pm 0.08$ and $\Gamma_{\text{ph}} = -2.05 \pm 0.10$ respectively (Fig. 2 and Fig. 3). The 10-1000 keV light curve in Extended Data Fig. 1 (panel c) was constructed by summing photon counts for the bright NaI detectors.

Swift/BAT The 15 – 350 keV mask-weighted light curve of the Burst Alert Telescope (BAT⁴¹) shows a multi-peaked structure that starts at $T_0 - 7$ s (Extended Data Fig. 1, panel b). The 68 – 110 s and 110 – 180 s spectra shown in Figs. 2 and 3 were derived from joint XRT-BAT fit. The best-fitting parameters for the whole interval (68 – 180 s) are: column density $N_{\text{H}} = (7.53^{+0.74}_{-1.74}) \times 10^{22} \text{ cm}^{-2}$ at $z = 0.42$, in addition to the galactic value of $7.5 \times 10^{19} \text{ cm}^{-2}$, low-energy photon index $\Gamma_{\text{ph},1} = -1.21^{+0.40}_{-1.26}$, high-energy spectral index $\Gamma_{\text{ph},2} = -2.19^{+0.39}_{-0.19}$, peak energy $E_{\text{pk}} > 14.5 \text{ keV}$. Errors are given at 90% confidence level.

Fermi/LAT The *Fermi* Large Area Telescope (LAT)⁴² detected a gamma-ray counterpart since the prompt phase⁴³. The burst left the LAT field of view (FoV) at T_0+150 s and remained outside

the LAT FoV until T_0+8600 s. The count light curve in the energy range 0.1-10 GeV is shown in Extended Data Fig. 1 (panel f). The LAT spectra in the time bins 68–110 s and 110–180 s (Figs. 2 and 3) are described by a power law with pivot energies of, respectively, 200 MeV and 500 MeV, photon indices $\Gamma_{\text{ph}}(68 - 110) = -2.02 \pm 0.95$ and $\Gamma_{\text{ph}}(110 - 180) = -1.69 \pm 0.42$, and corresponding normalisations of $N_{0,68-110} = (2.02 \pm 1.31) \times 10^{-7} \text{ ph MeV}^{-1} \text{ cm}^{-2} \text{ s}$ and $N_{0,110-180} = (4.48 \pm 2.10) \times 10^{-8} \text{ ph MeV}^{-1} \text{ cm}^{-2} \text{ s}$. In each time-interval, the analysis has been performed limited to the energy range where photons have been detected. The LAT light curve integrated in the energy range 0.1-1 GeV is shown in Fig. 1.

MAGIC We used the Major Atmospheric Gamma Imaging Cherenkov (MAGIC) standard software⁴⁴ and followed the steps optimised for the data taking under moderate moon illumination⁴⁵ to analyse the data. The spectral fitting is performed by a forward-folding method assuming a simple power law for the intrinsic spectrum and taking into account the **extragalactic background light** (EBL) effect using the model of Domínguez et al.⁴⁶. Extended Data Table 1 shows the fitting results for various time bins (the pivot energy is chosen to minimise the correlation between normalisation and photon index parameters). The data points shown in both Fig. 2 and 3 are obtained from the observed excess rates in estimated energy whose fluxes are evaluated in true energy using effective time and a spill-over corrected effective area obtained as a resultant of the best fit.

The time resolved analysis hints to a possible spectral evolution to softer values. Although we can not exclude that the photon indices are compatible with a constant value of ~ -2.5 up to 2400 s. The signal and background in the considered time bins are both in the low-count Poisson regime. Therefore, the correct treatment of the MAGIC data provided here includes along with the

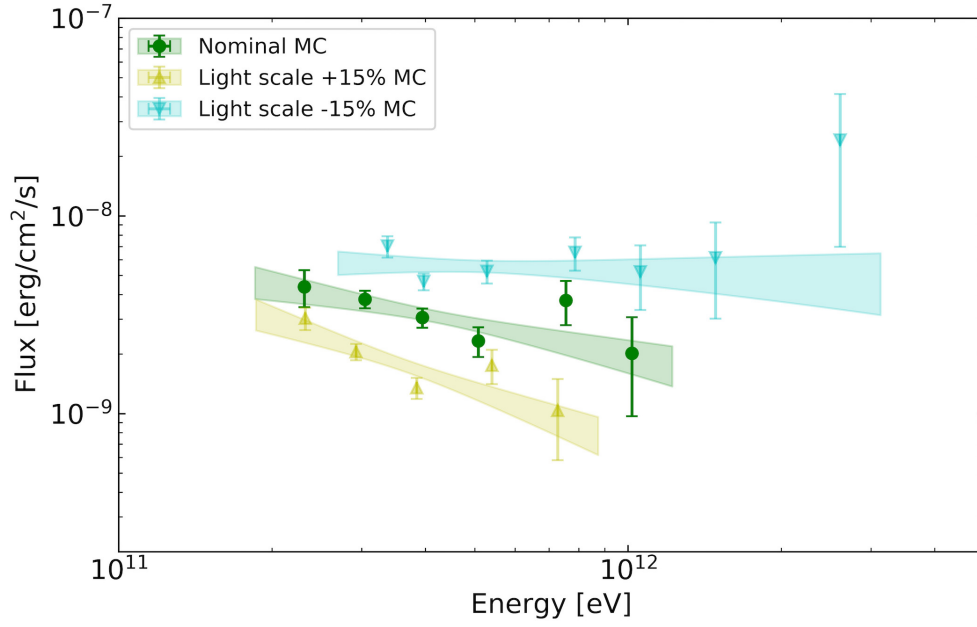
Time bin	Normalisation	Photon index	Pivot energy
[seconds after T_0]	[$\text{TeV}^{-1} \text{ cm}^{-2} \text{ s}^{-1}$]		[GeV]
62 - 90	$1.95^{+0.21}_{-0.20} \cdot 10^{-7}$	$-2.17^{+0.34}_{-0.36}$	395.5
68 - 180	$1.10^{+0.09}_{-0.08} \cdot 10^{-7}$	$-2.27^{+0.24}_{-0.25}$	404.7
180 - 625	$2.26^{+0.21}_{-0.20} \cdot 10^{-8}$	$-2.56^{+0.27}_{-0.29}$	395.5
68 - 110	$1.74^{+0.16}_{-0.15} \cdot 10^{-7}$	$-2.16^{+0.29}_{-0.31}$	386.5
110 - 180	$8.59^{+0.95}_{-0.91} \cdot 10^{-8}$	$-2.51^{+0.37}_{-0.41}$	395.5
180 - 360	$3.50^{+0.38}_{-0.36} \cdot 10^{-8}$	$-2.36^{+0.34}_{-0.37}$	395.5
360 - 625	$1.65^{+0.23}_{-0.23} \cdot 10^{-8}$	$-3.16^{+0.48}_{-0.54}$	369.1
625 - 2400	$3.52^{+0.47}_{-0.47} \cdot 10^{-9}$	$-2.80^{+0.48}_{-0.54}$	369.1
62 - 2400 (Nominal MC)	$1.07^{+0.08}_{-0.07} \cdot 10^{-8}$	$-2.51^{+0.20}_{-0.21}$	423.8
62 - 2400 (Light scale +15% MC)	$7.95^{+0.58}_{-0.56} \cdot 10^{-9}$	$-2.91^{+0.23}_{-0.25}$	369.1
62 - 2400 (Light scale -15% MC)	$1.34^{+0.09}_{-0.09} \cdot 10^{-8}$	$-2.07^{+0.18}_{-0.19}$	509.5

Extended Data Table 1: **MAGIC spectral fit parameters for GRB 190114C**. For each time bin, columns represent a) start time and end time of the bin; b) normalisation of the EBL-corrected differential flux at the pivot energy with statistical errors; c) photon indices with statistical errors; d) pivot energy of the fit (fixed).

460 use of the Poisson statistic also the systematic errors. To estimate the main source of systematic
 461 error caused by our imperfect knowledge of the absolute instrument calibration and the total at-
 462 mospheric transmission we vary the light-scale in our Monte Carlo (MC) simulation as suggested
 463 in previous studies⁴⁴. The result is reported in the last two lines of Extended Data Table 1 and in
 464 Extended Data Fig. 2.

465 The systematic effects deriving from the choice of one particular EBL model were also stud-
 466 ied. The analysis performed to obtain the time integrated spectrum was repeated employing other
 467 three models^{47–49}. The contribution to the systematic error on the photon index caused by the un-
 468 certainty on the EBL model is $\sigma_\alpha = {}^{+0.10}_{-0.13}$ which is smaller than the statistical error only (1 standard
 469 deviation) as already seen in a previous work¹⁰. On the other hand, the contribution to the system-
 470 atic error on the normalisation, due to choice of the EBL model, is only partially at the same level
 471 of the statistical error (1 standard deviation) $\sigma_N = {}^{+0.30}_{-0.08} \times 10^{-8}$. The chosen EBL model returns a
 472 lower normalisation with respect to two of the other models and very close to the third one⁴⁷.

473 The MAGIC energy flux light curve that is presented in Fig. 1 was obtained by integrating
 474 the best fit spectral model of each time bin from 0.3 to 1 TeV, in the same manner as a previous
 475 publication¹⁰. The value of the fitted time constant reported here differs less than two standard
 476 deviation from the one previously reported¹⁰. The difference is due to the poor constraints on the
 477 spectral fit parameters of the last time bin, which influences the light curve fit.



Extended Data Figure 2: **MAGIC time integrated spectral energy distributions in the time interval 62-2400 s after T_0 .** The green (yellow, blue) points and band show the result with the nominal (+15%, -15%) light scale MC, defining the limits of the systematic uncertainties. **The contour regions are drawn from the $1\text{-}\sigma$ error of their best-fit power law functions. The vertical bars of the data points show the $1\text{-}\sigma$ errors on the flux.**

X-ray afterglow observations

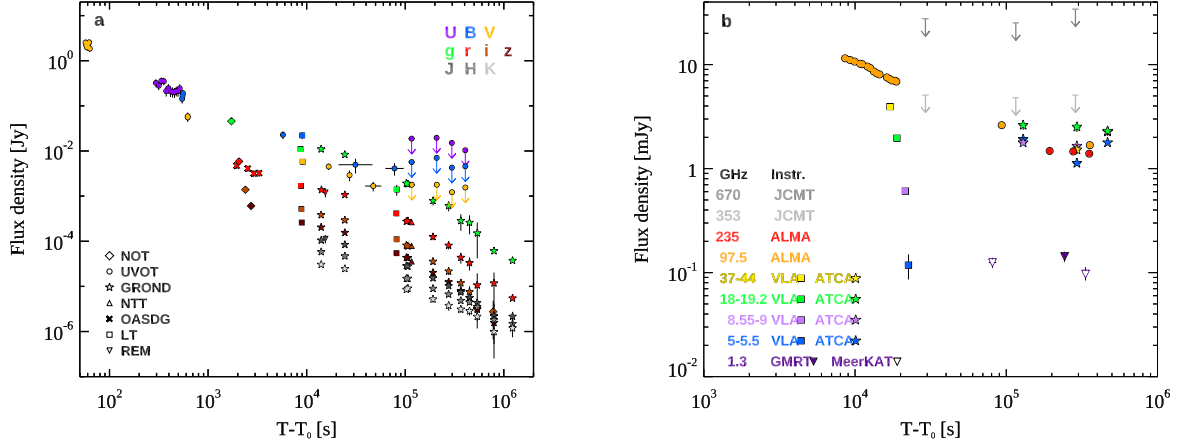
Swift/XRT The *Swift* X-Ray Telescope (XRT) started observing 68 s after T_0 . The source light curve⁵⁰ was taken from the *Swift*/XRT light curve repository⁵¹ and converted into 1-10 keV flux (Fig. 1) through dedicated spectral fits. The combined spectral fit XRT+BAT in Figs. 2 and 3 has been described above.

XMM-Newton and NuSTAR The *XMM-Newton* X-ray Observatory and the Nuclear Spectroscopic Telescope Array (*NuSTAR*) started observing GRB 190114C under DDT ToOs 7.5 hours and 22.5 hrs (respectively) after the burst. The *XMM-Newton* and NuSTAR absorption-corrected fluxes (see Fig. 1) were derived by fitting the spectrum with XSPEC adopting the same power law model, with absorption in our Galaxy and at the redshift of the burst.

NIR, Optical and UV afterglow observations Light curves from the different instruments presented in this section are shown in Extended Data Fig. 3.

GROND The Gamma-ray Burst Optical/Near-infrared Detector (GROND⁵²) started observations 3.8 hours after the GRB trigger, and the follow-up continued until January 29, 2019. Image reduction and photometry were carried out with standard IRAF tasks⁵³, as described in^{54,55}. JHK_s photometry was converted to AB magnitudes to have a common flux system. Final photometry is given in Extended Data Table 2.

GTC The BOOTES-2 ultra-wide field camera⁵⁶, took an image at the GRB 190114C location, starting at 20:57:18 UT (30 s exposure time) (see Extended Data Fig. 4). The Gran Canarias



Extended Data Figure 3: **Afterglow light curves of GRB 190114C.** Flux density at different frequencies, as a function of the time since the initial burst T_0 . Panel **a**: observations in the NIR/Optical/UV bands. The flux has been corrected for extinction in the host and in our Galaxy. The contribution of the host galaxy and its companion has been subtracted. Fluxes have been rescaled (except for the r filter). Panel **b**: Radio and sub-mm observations from 1.3 GHz to 670 GHz.

T_{GROND}	AB magnitude						
(s)	g'	r'	i'	z'	J	H	K_s
14029.94 \pm 335.28	19.21 \pm 0.03	18.46 \pm 0.03	17.78 \pm 0.03	17.33 \pm 0.03	16.78 \pm 0.05	16.30 \pm 0.05	16.03 \pm 0.07
24402.00 \pm 345.66	19.50 \pm 0.04	18.72 \pm 0.03	18.05 \pm 0.03	17.61 \pm 0.03	17.02 \pm 0.05	16.53 \pm 0.05	16.26 \pm 0.08
102697.17 \pm 524.01	20.83 \pm 0.06	20.00 \pm 0.04	19.30 \pm 0.04	18.87 \pm 0.03	18.15 \pm 0.05	17.75 \pm 0.06	17.40 \pm 0.09
106405.63 \pm 519.87	20.86 \pm 0.05	19.98 \pm 0.03	19.34 \pm 0.03	18.88 \pm 0.03	18.17 \pm 0.06	17.75 \pm 0.06	17.34 \pm 0.09
191466.77 \pm 751.37	21.43 \pm 0.07	20.61 \pm 0.03	19.97 \pm 0.03	19.52 \pm 0.03	18.77 \pm 0.06	18.28 \pm 0.06	17.92 \pm 0.14
275594.19 \pm 747.59	21.57 \pm 0.07	20.88 \pm 0.04	20.31 \pm 0.04	19.87 \pm 0.04	19.14 \pm 0.07	18.57 \pm 0.06	18.26 \pm 0.21
366390.74 \pm 1105.79	21.87 \pm 0.07	21.17 \pm 0.04	20.62 \pm 0.03	20.15 \pm 0.03	19.43 \pm 0.06	18.89 \pm 0.06	18.46 \pm 0.15
448791.55 \pm 1201.33	21.90 \pm 0.08	21.27 \pm 0.04	20.79 \pm 0.04	20.33 \pm 0.03	19.66 \pm 0.07	18.97 \pm 0.07	18.55 \pm 0.18
537481.41 \pm 1132.16	22.02 \pm 0.09	21.52 \pm 0.05	21.00 \pm 0.04	20.55 \pm 0.03	19.87 \pm 0.07	19.20 \pm 0.07	18.83 \pm 0.17
794992.63 \pm 1200.69	22.14 \pm 0.04	21.51 \pm 0.03	21.05 \pm 0.04	20.71 \pm 0.05	20.31 \pm 0.13	19.79 \pm 0.14	19.59 \pm 0.41
1226716.84 \pm 1050.15	22.17 \pm 0.04	21.59 \pm 0.04	21.26 \pm 0.04	20.97 \pm 0.04	20.34 \pm 0.12	19.95 \pm 0.11	19.40 \pm 0.34

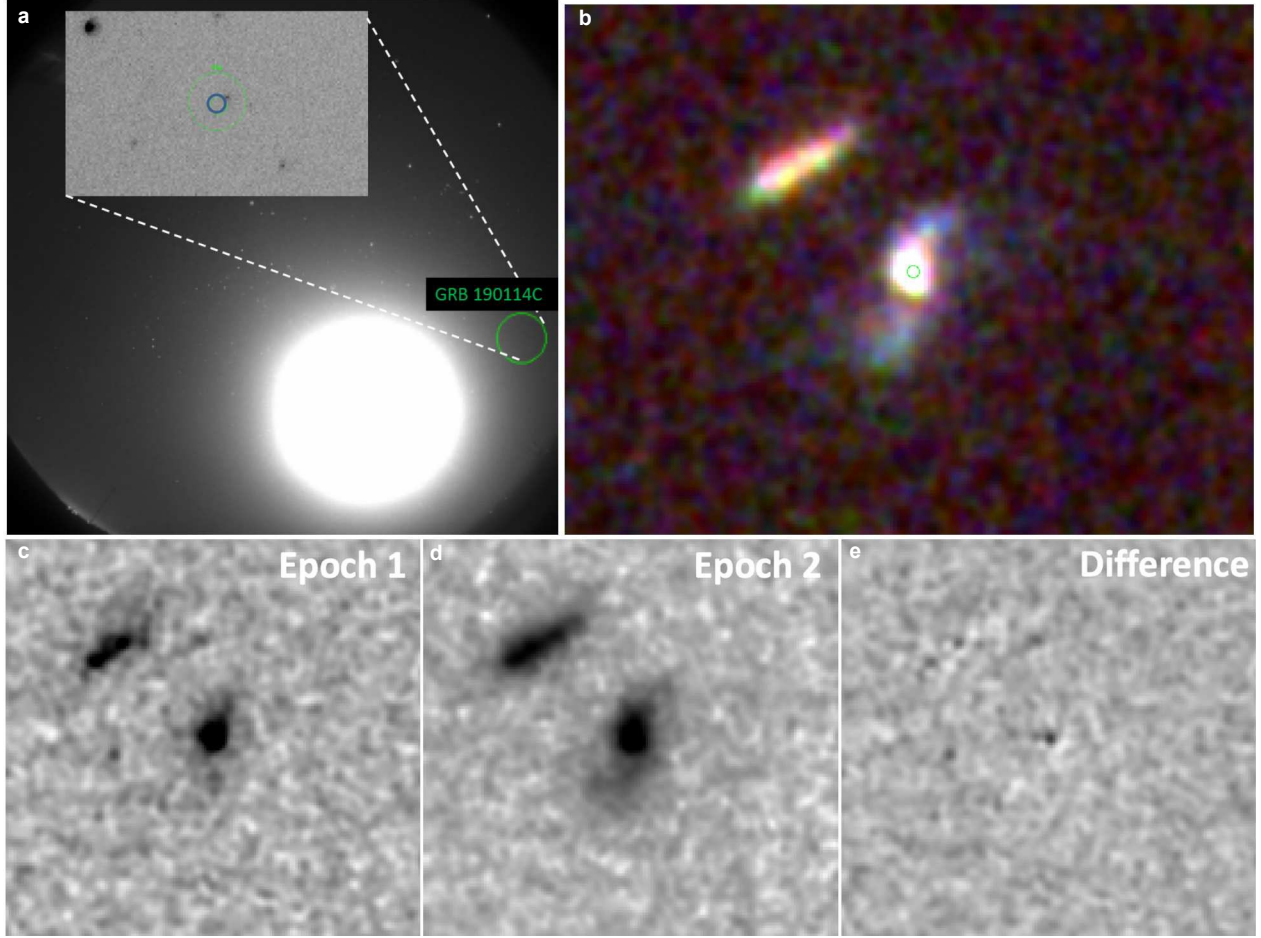
Extended Data Table 2: **GROND photometry.** T_{GROND} in seconds after the BAT trigger. The AB magnitudes are not corrected for the Galactic foreground reddening.

Telescope (GTC) equipped with the OSIRIS spectrograph⁵⁷ started observations 2.6 hr post-burst. The grisms R1000B and R2500I were used covering the wavelength range 3,700-10,000 Å (600 s exposure times for each grism). The GTC detects a highly extinguished continuum, as well as CaII H and K lines in absorption, and [OII], H β , and [OIII] in emission (see Extended Data Fig. 5), all roughly at the same redshift $z = 0.4245 \pm 0.0005$ ⁵⁸. Comparing the derived rest-frame equivalent widths (EWs) with the work by⁵⁹, GRB 190114C clearly shows higher than average, but not unprecedented, values.

HST The *Hubble Space Telescope* (HST) imaged the afterglow and host galaxy of GRB 190114C on 11 February and 12 March 2019. HST observations clearly reveal that the host galaxy is spiral (Extended Data Fig. 4). A direct subtraction of the epochs of F850LP observations yields a faint residual close to the nucleus of the host (Extended Data Fig. 4). From the position of the residual we estimate that the burst originated within 250 pc of the host galaxy nucleus.

LT The robotic 2-m Liverpool Telescope (LT⁶⁰) slewed to the afterglow location at UTC 2019-01-14.974 and on the second night, from UTC 2019-01-15.814 and acquired images in B , g , V , r , i and z bands (45 s exposure each in the first night and 60 s in the second, see Extended Data Table 3). Aperture photometry of the afterglow was performed using a custom IDL script with a fixed aperture radius of 1.5". Photometric calibration was performed relative to stars from the Pan-STARRS1 catalogue⁶¹.

NTT The ESO New Technology Telescope (NTT) observed the optical counterpart of GRB 190114C under the extended Public ESO Spectroscopic Survey for Transient Objects (ePESSTO) using the



Extended Data Figure 4: **Images of the localisation region of GRB 190114C.** Panel **a**: The CASANDRA-2 at the BOOTES-2 station all-sky image. The image (30 s exposure, unfiltered) was taken at $T_0+14.8$ s. At the GRB 190114C location (circle) no prompt optical emission is detected. Panel **b**: Three-colour image of the host of GRB 190114C with the HST. The host galaxy is a spiral galaxy, and the green circle indicates the location of the transient close to its host nucleus. The image is $8''$ across, north is up and east to the left. Panels **c**, **d** and **e**: F850LP imaging of GRB 190114C taken with the HST. Two epochs are shown (images are $4''$ across), as well as the result of the difference image. A faint transient is visible close to the nucleus of the galaxy, and we identify this as the late time afterglow of the burst.

UTC	Filter	Exposure (s)	Magnitude
LT/O:O			
2019-01-14.975	<i>g</i>	45	19.08±0.06
2019-01-14.976	<i>r</i>	45	18.22±0.02
2019-01-14.977	<i>i</i>	45	17.49±0.02
2019-01-14.978	<i>z</i>	45	17.12±0.02
2019-01-14.979	<i>B</i>	45	19.55±0.15
2019-01-14.980	<i>V</i>	45	18.81±0.08
2019-01-15.814	<i>r</i>	60	19.61±0.05
2019-01-15.818	<i>z</i>	60	18.70±0.06
2019-01-15.820	<i>i</i>	60	19.04±0.04
2019-01-15.823	<i>g</i>	60	20.96±0.17
NOT/aIFOSC			
2019-01-14.89127	<i>g</i>	1 × 300	17.72±0.03
2019-01-14.89512	<i>r</i>	1 × 300	16.93±0.02
2019-01-14.89899	<i>i</i>	1 × 300	16.42 ±0.04
2019-01-14.90286	<i>z</i>	1 × 300	16.17 ±0.04
2019-01-23.8896	<i>i</i>	6 × 300	21.02±0.05

UVOT							
T_{start}	T_{stop}	Filter	Magnitude	T_{start}	T_{stop}	Filter	Magnitude
56.63	57.63	<i>V</i>	12.17±0.14	130958	142524	<i>UVM2</i>	20.37
57.63	58.63	<i>V</i>	12.34±0.14	217406	222752	<i>UVM2</i>	20.48
58.63	59.63	<i>V</i>	12.44±0.13	107573	125233	<i>U</i>	20.29
59.63	60.63	<i>V</i>	12.29±0.14	205500	210750	<i>U</i>	20.25
60.63	61.63	<i>V</i>	12.44±0.14	291188	302718	<i>U</i>	20.49
61.63	62.63	<i>V</i>	12.16±0.13	400429	412385	<i>U</i>	20.82
62.63	63.63	<i>V</i>	12.51±0.13	616	627	<i>V</i>	16.25±0.20
615.95	625.95	<i>V</i>	16.32±0.20	16295	17136	<i>V</i>	19.03±0.14
73.34	83.34	<i>white</i>	13.86	26775	27682	<i>V</i>	19.50±0.27
83.34	93.34	<i>white</i>	14.10±0.06	39149	57221	<i>V</i>	20.09±0.23
93.34	103.34	<i>white</i>	14.19±0.06	108064	125736	<i>V</i>	20.02
103.34	113.34	<i>white</i>	14.36±0.06	206689	211356	<i>V</i>	20.02
113.34	123.34	<i>white</i>	14.64±0.06	292383	303996	<i>V</i>	20.42
123.34	133.34	<i>white</i>	14.65±0.06	401305	413316	<i>V</i>	20.17
133.34	143.34	<i>white</i>	14.91±0.06	4044	51522	<i>UVW1</i>	21.17
143.34	153.34	<i>white</i>	14.99±0.06	131216	142656	<i>UVW1</i>	20.47
153.34	163.34	<i>white</i>	15.05±0.06	217984	223056	<i>UVW1</i>	20.57
163.34	173.34	<i>white</i>	15.32±0.06	592	612	<i>UVW2</i>	17.65
173.34	183.34	<i>white</i>	15.38±0.06	6056	56384	<i>UVW2</i>	21.30
183.34	193.34	<i>white</i>	15.38±0.06	130699	142346	<i>UVW2</i>	20.52
193.34	203.34	<i>white</i>	15.59±0.06	216828	222404	<i>UVW2</i>	20.55
562.0	572.0	<i>white</i>	16.96±0.10	566	586	<i>white</i>	16.90±0.07
572.0	582.0	<i>white</i>	16.90±0.10	607389	613956	<i>white</i>	22.16
535.5	555.5	<i>B</i>	17.56±0.21	624452	682416	<i>white</i>	21.99±0.18
545.5	565.5	<i>B</i>	17.25±0.18	745033	769296	<i>white</i>	21.64±0.16
285.9	305.9	<i>U</i>	17.35±0.19	818840	837216	<i>white</i>	22.50
305.9	325.9	<i>U</i>	17.50±0.20	893522	907116	<i>white</i>	22.57
325.9	345.9	<i>U</i>	17.24±0.18	991065	1004196	<i>white</i>	22.49±0.35
345.9	365.9	<i>U</i>	17.26±0.18	1077542	1094616	<i>white</i>	22.41±0.31
365.9	385.9	<i>U</i>	17.80±0.24	1140343	1170336	<i>white</i>	22.50
385.9	405.9	<i>U</i>	17.64±0.22	1220661	1274376	<i>white</i>	22.36±0.29
405.9	425.9	<i>U</i>	17.82±0.24	5851	6050	<i>white</i>	19.25±0.09
425.9	445.9	<i>U</i>	17.84±0.25	21950	22857	<i>white</i>	20.25±0.09
445.9	465.9	<i>U</i>	17.87±0.25	1353459	1359284	<i>white</i>	21.70
465.9	485.9	<i>U</i>	17.79±0.24	1502211	1548336	<i>white</i>	21.98±0.24
485.9	505.9	<i>U</i>	17.81±0.24	1692292	1703935	<i>white</i>	22.07
505.9	525.9	<i>U</i>	17.65±0.22	2132978	2146056	<i>white</i>	22.58
542	561	<i>B</i>	17.38±0.14	2299521	2317956	<i>white</i>	22.41±0.31
5646	5845	<i>B</i>	19.54±0.19	63686	80942	<i>white</i>	21.07±0.24
21038	46521	<i>B</i>	21.14±0.35	107900	125591	<i>white</i>	21.40±0.28
62774	96486	<i>B</i>	21.33±0.29	206292	211137	<i>white</i>	21.52
107737	125412	<i>B</i>	21.00	291984	303556	<i>white</i>	21.48±0.23
205896	210944	<i>B</i>	20.78	401012	413029	<i>white</i>	21.84
291586	303137	<i>B</i>	21.29	491973	505356	<i>white</i>	22.21±0.24
400721	412707	<i>B</i>	21.22	74	224	<i>white</i>	14.90±0.02
3839	50615	<i>UVM2</i>	20.88±0.28				

Extended Data Table 3: Liverpool Telescope, Nordic Optical Telescope, and UVOT observations. Magnitudes are SDSS AB-"like" for ugriz, Vega-"like" for all the other filters and are not corrected for Galactic extinction. For UVOT data, magnitudes without uncertainties are upper limits.

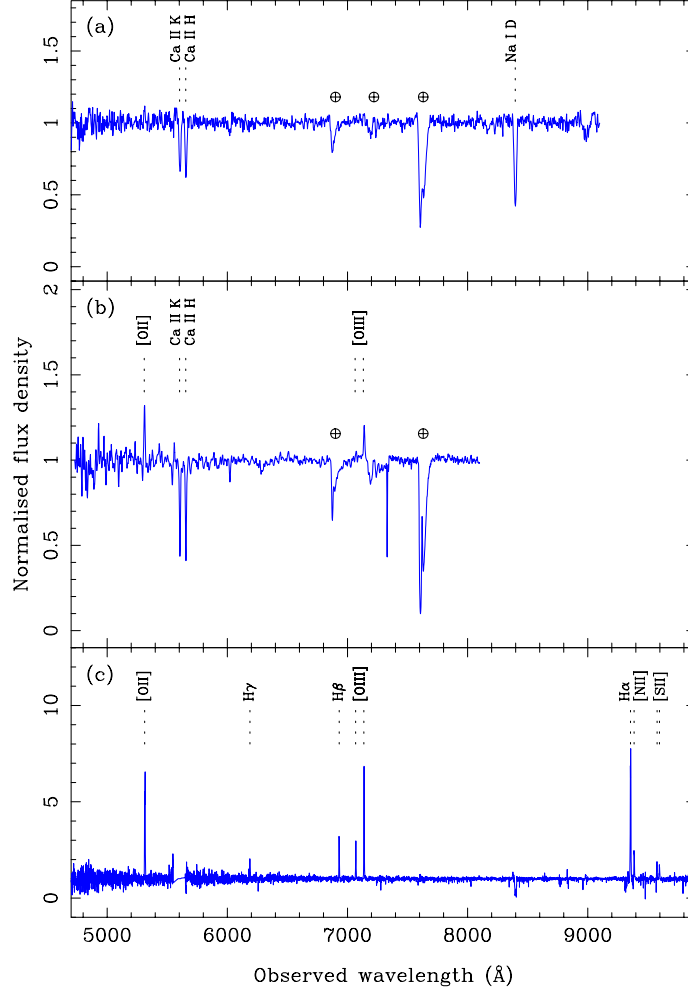
517 NTT/EFOSC2 instrument in imaging mode⁶². Observations started at 04:36:53 UT on 2019 Jan-
518 uary 16 with the g , r , i , z Gunn filters. Image reduction was carried out by following the standard
519 procedures⁶³.

520 **OASDG** The 0.5 m remote telescope of the Osservatorio Astronomico “S. Di Giacomo” (OASDG),
521 located in Agerola (Italy) started observations in the optical Rc -band 0.54 hours after the burst. The
522 afterglow of GRB 190114C was clearly detected in all the images.

523 **NOT** The Nordic Optical Telescope (NOT) observed the optical afterglow of GRB 190114C with
524 the Alhambra Faint Object Spectrograph and Camera (AlFOSC) instrument. Imaging was obtained
525 in the $griz$ filters with 300 s exposures, starting at Jan 14 21:20:56 UT, 24 minutes after the BAT
526 trigger. The normalised spectrum (Extended Data Fig. 5) reveals strong host interstellar absorption
527 lines due to Ca H & K and Na ID, which provided a redshift of $z = 0.425$.

528 **REM** The Rapid Eye Mount telescope (REM) performed optical and NIR observations with
529 the REM 60 cm robotic telescope equipped with the ROS2 optical imager and the REMIR NIR
530 camera⁶⁴. Observations were performed starting about 3.8 hours after the burst in the r , and J
531 bands and lasted about one hour.

532 **Swift/UVOT** The *Swift* UltraViolet and Optical Telescope (UVOT⁶⁵) began observations at $T_0 + 54$
533 seconds in the UVOT v band. The first observation after settling started 74 s after the trigger for
534 150 s in the UVOT *white* band⁶⁶. A 50 s exposure with the UV grism was taken thereafter, followed
535 by multiple exposures rotating through all seven broad and intermediate-band filters until switching
536 to only UVOT’s clear white filter on 2019-01-20. Standard photometric calibration and methods



Extended Data Figure 5: **Optical/NIR spectra of GRB 190114C.** Panel **a**: The NOT/AIFOSC spectrum obtained at a mid-time 1 hr post-burst. The continuum is afterglow dominated at this time, and shows strong absorption features of Ca II and Na I (in addition to telluric absorption). Panel **b**: the normalised GTC (+OSIRIS) spectrum on Jan 14, 23:32:03 UT, with the R1000B and R2500I grisms. The emission lines of the underlying host galaxy are noticeable, besides the Ca II absorption lines in the afterglow spectrum. Panel **c**: The visible light region of the VLT/X-shooter spectrum obtained approximately 3.2 d post-burst, showing strong emission lines from the star-forming host galaxy.

were used for deriving the aperture photometry^{67,68}. The grism zeroth order the data were reduced manually⁶⁹ to derive the b -magnitude and error.

VLT The STARGATE collaboration used the Very Large Telescope (VLT) and observed GRB 190114C using the X-shooter spectrograph. Detailed analysis will be presented in forthcoming papers. A portion of the second spectrum is shown in Extended Data Fig. 5, illustrating the strong emission lines characteristic of a strongly star-forming galaxy, whose light is largely dominating over the afterglow at this epoch.

Magnitudes of the underlying galaxies The *HST* images show a spiral or tidally disrupted galaxy whose bulge is coincident with the coordinates of GRB 190114C. A second galaxy is detected at an angular distance of $1.3''$, towards the North East. The SED analysis was performed with LePhare^{70,71} using an iterative method that combined both the resolved photometry of the two galaxies found in the *HST* and *VLT/HAWK-I* data and the blended photometry from *GALEX* and *WISE*, where the spatial resolution was much lower. Further details will be given in a paper in preparation (de Ugate Postigo et al.). The estimated photometry, for each object and their combination, is given in Extended Data Table 4.

Optical Extinction The optical extinction toward the line of sight of a GRB is derived assuming a power law as intrinsic spectral shape⁷². Once the Galactic extinction ($E_{B-V} = 0.01$ ⁷³) is taken into account and the fairly bright host galaxy contribution is properly subtracted, a good fit to the data is obtained with the LMC recipe and $A_V = 1.83 \pm 0.15$. The spectral index β ($F_\nu \propto \nu^{\beta_0}$) evolves from hard to soft across the temporal break in the optical light-curve at about 0.5 days,

Filter	Host	Companion	Combined
Sloan u	23.54	25.74	23.40
Sloan g	22.51	23.81	22.21
Sloan r	22.13	22.81	21.66
Sloan i	21.70	22.27	21.19
Sloan z	21.51	21.74	20.87
2MASS J	20.98	21.08	20.28
2MASS H	20.68	20.82	20.00
2MASS K_s	20.45	20.61	19.77

Extended Data Table 4: **Observations of the host galaxy.** For each filter, the estimated magnitudes are given for the host galaxy of GRB 190114C, the companion and the combination of the two objects.

557 moving from $\beta_{o,1} = -0.10 \pm 0.12$ to $\beta_{o,2} = -0.48 \pm 0.15$.

558 **Radio and Sub-mm afterglow observations** The light curves from the different instruments are
559 shown in Extended Data Fig. 3.

560 **ALMA** The Atacama Large Millimetre/Submillimetre Array (ALMA) observations are reported
561 in Band 3 (central observed frequency of 97.500 GHz) and Band 6 (235.0487 GHz), between 2019
562 January 15 and 2019 January 19. Data were calibrated within CASA (Common Astronomy Soft-
563 ware Applications, version 5.4.0⁷⁴) using the pipeline calibration. Photometric measurements were
564 also performed within CASA. ALMA early observations at 97.5 GHz are taken from ¹⁵.

565 **ATCA** The Australia Telescope Compact Array (ATCA) observations were made with the ATCA
566 4 cm receivers (band centres 5.5 and 9 GHz), 15 mm receivers (band centres 17 and 19 GHz), and
567 7 mm receivers (band centres 43 and 45 GHz). ATCA data were obtained using the CABB con-
568 tinuum mode ⁷⁵ and reduced with the software packages MIRIAD ⁷⁶ and CASA ⁷⁴ using standard
569 techniques. The quoted errors are 1σ , which include the RMS and Gaussian 1σ errors.

570 **GMRT** The upgraded Giant Metre-wave Radio Telescope ⁷⁷ (UGMRT) observed on 17th January
571 2019 13.44 UT (2.8 days after the burst) in band 5 (1000-1450 MHz) with 2048 channels spread
572 over 400 MHz. GMRT detected a weak source with a flux density of $73 \pm 17 \mu\text{Jy}$ at the GRB
573 position ⁷⁸. The flux should be considered as an upper limit, as the contribution from the host ⁷⁹ has
574 not been subtracted.

ATCA			
Start Date and Time	End Date and Time	Frequency GHz	Flux mJy
1/16/2019 6:47:00	1/16/2019 10:53:00	5.5	1.92±0.06
		9	1.78±0.06
		18	2.62±0.26
1/18/2019 1:45:00	1/18/2019 11:18:00	5.5	1.13±0.04
		9	1.65±0.05
		18	2.52±0.27
		44	1.52±0.15
1/20/2019 3:38	1/20/2019 10:25:00	5.5	1.78±0.06
		9	2.26±0.07
		18	2.30±0.23

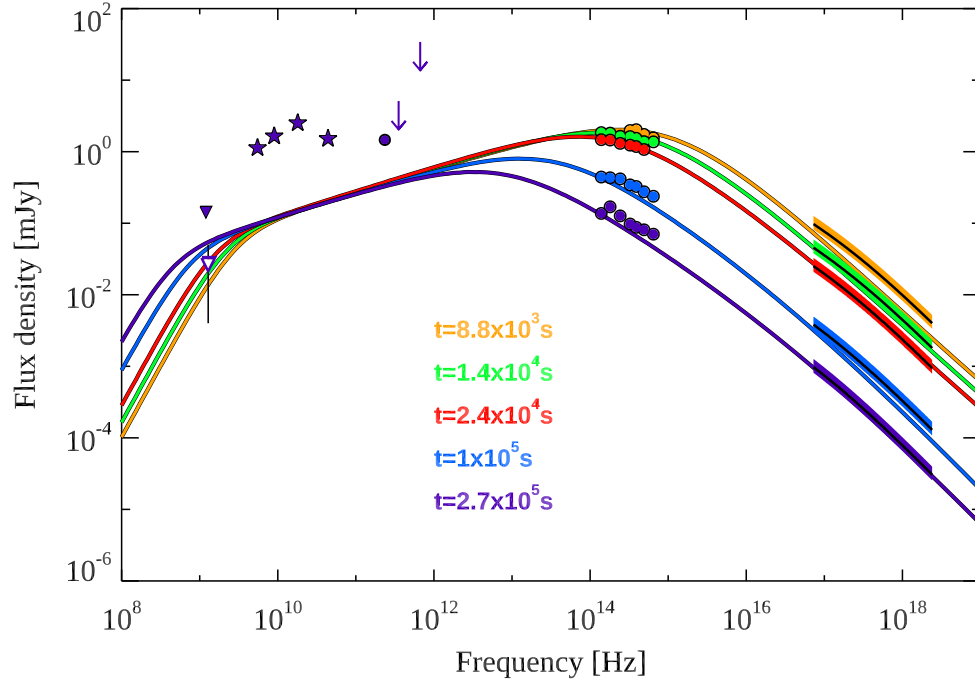
JCMT SCUBA-2						
UT Date	Time since trigger (days)	Time on source (hours)	Typical 225 GHz CSO Opacity	Typical elevation (degrees)	850 μ m RMS density (mJy/beam)	450 μ m RMS density (mJy/beam)
2019-01-15	0.338	1.03	0.026	39	1.7	9.2
2019-01-16	1.338	1.03	0.024	39	1.6	8.4
2019-01-18	3.318	0.95	0.031	37	1.7	11.4

Extended Data Table 5: **Observations of GRB 190114C by ATCA and JCMT SCUBA-2.** For ATCA data, start and end date and times (UTC) of the observations, frequency, and flux (1σ error) are reported. For JCMT SCUBA-2 data, the CSO 225 GHz opacity measures the zenith atmospheric attenuation.

MeerKAT The new MeerKAT radio observatory^{80,81} observed on 15 and 18 January 2019, with DDT requested by the ThunderKAT Large Survey Project⁸². Both epochs used 63 antennas and were done at L-band spanning 856 MHz and centered at 1284 MHz. MeerKAT flux estimation was done by finding and fitting the source with the software PyBDSF v.1.8.15⁸³. Adding the RMS noise in quadrature to the flux uncertainty leads to final flux measurements of $125 \pm 14 \mu\text{Jy/beam}$ on 15 January and $97 \pm 16 \mu\text{Jy/beam}$ on 18 January. The contribution from the host galaxy⁷⁹ has not been subtracted. Therefore, these measurements provide a maximum flux of the GRB.

JCMT SCUBA-2 Sub-millimeter Sub-millimeter observations were performed simultaneously at $850 \mu\text{m}$ and $450 \mu\text{m}$ on three nights using the SCUBA-2 continuum camera⁸⁴. GRB 190114C was not detected on any of the individual nights. Combining all the SCUBA-2 continuum camera⁸⁴ observations, the RMS background noise is 0.95 mJy/beam at $850 \mu\text{m}$ and 5.4 mJy/beam at $450 \mu\text{m}$ at 1.67 days after the burst trigger.

Prompt emission model for the early time MAGIC emission In the standard picture the prompt sub-MeV spectrum is explained as a synchrotron radiation from relativistic accelerated electrons in the energy dissipation region. The associated inverse Compton component is sensitive to the details of the dynamics: e.g. in the internal shock model if the peak energy is initially very high and the IC component is suppressed due to Klein-Nishina (KN) effects, the peak of the IC component may be delayed and become bright only at late times when scatterings occur in Thomson regime. Simulations showed that magnetic fields required to produce the GeV/TeV component are rather low⁸⁵, $\epsilon_B \sim 10^{-3}$. In this framework the contribution of the IC component to the observed flux at early times (62-90 s, see Extended Data Table 1) does not exceed $\sim 20\%$. Alternatively, if



Extended Data Figure 6: **Radio to X-rays SED at different epochs.** The synchrotron frequency ν_m crosses the optical band, moving from higher to lower frequencies. The break between 10^8 and 10^{10} Hz is caused by the self-absorption synchrotron frequency ν_{sa} . Optical (X-ray) data have been corrected for extinction (absorption).

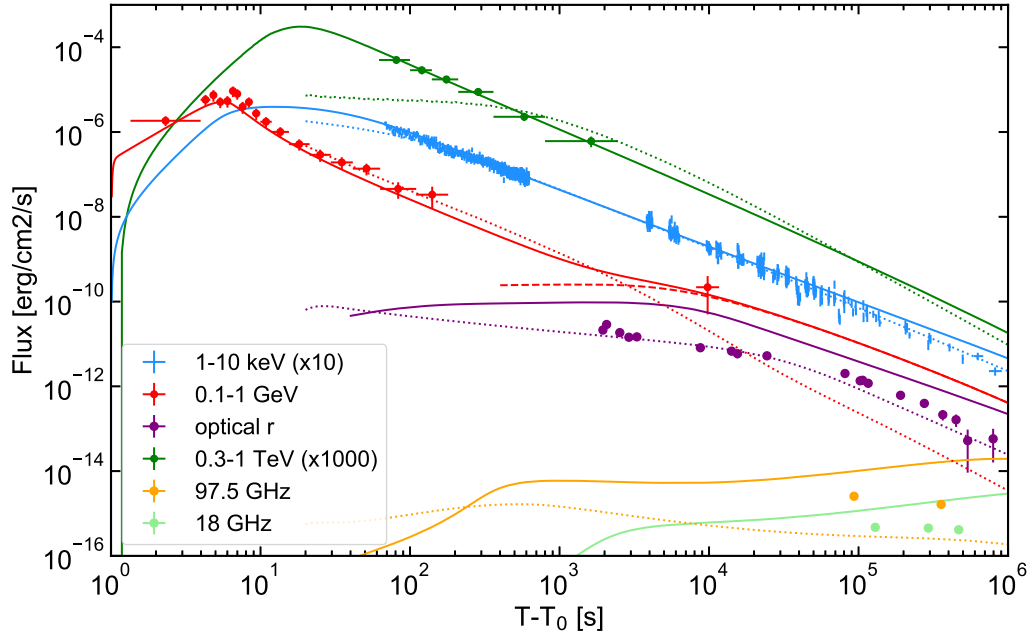
the prompt emission originates in reprocessed photospheric emission, the early TeV flux may arise from IC scatterings of thermal photons by freshly heated electrons below the photosphere at low optical depths. Another possibility for the generation of TeV photons might be the inverse Compton scattering of prompt MeV photons by electrons in the external forward shock region where electrons are heated to an average Lorentz factor of order 10^4 at early times.

Afterglow model Synchrotron and SSC radiation from electrons accelerated at the forward shock has been modelled within the external shock scenario^{7,8,19,24,86}. The results of the modeling are overlaid to the data in Fig. 3, and Extended Data Figs. 6 and 7.

We consider two types of power law radial profiles $n(R) = n_0 R^{-s}$ for the external environment: $s = 0$ (homogeneous medium) and $s = 2$ (wind-like medium, typical of an environment shaped by the stellar wind of the progenitor). In the last case, we define $n_0 = 3 \times 10^{35} A_\star \text{ cm}^{-1}$. We assume that electrons swept up by the shock are accelerated into a power law distribution described by spectral index p : $dN/d\gamma \propto \gamma^{-p}$, where γ is the electron Lorentz factor. We call ν_m the characteristic synchrotron frequency of electrons with Lorentz factor γ_m , ν_c the cooling frequency, and ν_{sa} the synchrotron self-absorption frequency.

The early time optical emission (up to ~ 1000 s) and radio emission (up to $\sim 10^5$ s) are most likely dominated by reverse shock radiation¹⁵. Detailed modeling of this component is not discussed in this work, where we focus on forward shock radiation.

The XRT flux (Fig. 1, blue data points) decays as $F_X \propto t^{\alpha_X}$ with $\alpha_X = -1.36 \pm 0.02$. If $\nu_X > \max(\nu_m, \nu_c)$, the X-ray light curve is predicted to decay as $t^{(2-3p)/4}$, that implies $p \sim 2.5$.



Extended Data Figure 7: **Modeling of the broadband light curves.** Modeling of forward shock emission is compared to observations at different frequencies (see legend). The model shown with solid and dashed lines is optimised to describe the high-energy radiation (TeV, GeV and X-ray). It has been obtained with the following parameters: $s = 0$, $\epsilon_e = 0.07$, $\epsilon_B = 8 \times 10^{-5}$, $p = 2.6$, $n_0 = 0.5$, and $E_k = 8 \times 10^{53}$ erg. Solid lines show the total flux (synchrotron and SSC), while the dashed line refers to the SSC contribution only. Dotted curves are derived to test a better modeling of observations at lower frequencies, but fail to explain the behaviour of the TeV light curve. These are obtained with the following model parameters: $s = 2$, $\epsilon_e = 0.6$, $\epsilon_B = 10^{-4}$, $p = 2.4$, $A_\star = 0.1$, and $E_k = 4 \times 10^{53}$ erg.

Another possibility is to assume $\nu_m < \nu_X < \nu_c$, which implies $p = 2.1 - 2.2$ for $s = 2$ and $p \sim 2.8$ for $s = 0$. A broken power law fit provides a better fit (5.3×10^{-5} probability of chance improvement), with a break occurring around 4×10^4 s and decay indices $\alpha_{X,1} \sim -1.32 \pm 0.03$ and $\alpha_{X,2} \sim -1.55 \pm 0.04$. This behaviour can be explained by the passage of ν_c in the XRT band and assuming again $p = 2.4 - 2.5$ for $s = 2$ and $p \sim 2.8$ for $s = 0$.

The optical light curve starts displaying a shallow decay in time (with temporal index poorly constrained, between -0.5 and -0.25) starting from $\sim 2 \times 10^3$ s, followed by a steepening around 8×10^4 s, when the temporal decay becomes similar to the decay in X-ray band, suggesting that after this time the X-ray and optical band lie in the same part of the synchrotron spectrum. If the break is interpreted as the synchrotron characteristic frequency ν_m crossing the optical band, after the break the observed temporal decay requires a steep value of $p \sim 3$ for $s = 0$ and a value between $p = 2.4$ and $p = 2.5$ for $s = 2$. Independently of the density profile of the external medium and on the cooling regime of the electrons, $\nu_m \propto t^{-3/2}$, placing it the soft X-ray band at 10^2 s. The SED at ~ 100 s is indeed characterised by a peak in between 5-30 keV (Fig. 3). Information on the location of the self-absorption frequency are provided by observations at 1 GHz, showing that $\nu_{sa} \sim 1$ GHz at 10^5 s (Extended Data Fig. 6).

Summarizing, in a wind-like scenario X-ray and optical emission and their evolution in time can be explained if $p = 2.4 - 2.5$, the emission is initially in fast cooling regime and transitions to a slow cooling regime around 3×10^3 s. The optical spectral index at late times is predicted to be $(1 - p)/2 \sim -0.72$, in agreement with observations. ν_m crosses the optical band at $t \sim 8 \times 10^4$ s, explaining the steepening of the optical light curve and the flattening of the optical spectrum.

The X-ray band initially lies above (or close to) ν_m , and the break frequency ν_c starts crossing the X-ray band around $2 - 4 \times 10^4$ s, producing the steepening in the decay rate (the cooling frequency increases with time for $s = 2$). In this case, before the temporal break, the decay rate is related to the spectral index of the electron energy distribution by $\alpha_{X,1} = (2 - 3p)/4 \sim -1.3$, for $p \sim 2.4 - 2.5$. Well after the break, this value of p predicts a decay rate $\alpha_{X,1} = (1 - 3p)/4 = -1.55 - 1.62$. Overall, this interpretation is also consistent with the fact that the late time ($t > 10^5$ s) X-ray and optical light curves display similar temporal decays (Fig. 1), as they lie in the same part of the synchrotron spectrum ($\nu_m < \nu_{\text{opt}} < \nu_X < \nu_c$). A similar picture can be invoked to explain the emission also assuming a homogeneous density medium, but a steeper value of p is required. In this case, however, no break is predicted in the X-ray light curve.

We now add to the picture the information brought by the TeV detection. The modeling is built with reference to the MAGIC flux and spectral indices derived considering statistical errors only (see Extended Data Table 1 and green data points in Extended Data Fig. 2). The light curve decays in time as $t^{-1.51}$ and the photon index is consistent within $\sim 1\sigma$ with $\Gamma_{\text{ph,TeV}} \sim -2.5$ for the entire duration of the emission, although there is evidence for an evolution from harder (~ -2) to softer (~ -2.8) values. In the first broadband SED (Fig. 3, 68-110 s), LAT observations provide strong evidence for the presence of two separated spectral peaks.

Assuming Thomson scattering, the SSC peak is given by:

$$\nu_{\text{peak}}^{\text{SSC}} \simeq 2 \gamma_e^2 \nu_{\text{peak}}^{\text{syn}} \quad (1)$$

while in KN regime, the SSC peak should be located at:

$$h\nu_{\text{peak}}^{\text{SSC}} \simeq 2 \gamma_e \Gamma m_e c^2 / (1 + z) \quad (2)$$

where $\gamma_e = \min(\gamma_c, \gamma_m)$. The synchrotron spectral peak is located at $E_{\text{peak}}^{\text{syn}} \sim 10 \text{ keV}$, while the peak of the SSC component must be below $E_{\text{peak}}^{\text{SSC}} \lesssim 100 \text{ GeV}$ to explain the MAGIC photon index. Both the KN and Thomson scattering regimes imply $\gamma_e \lesssim 10^3$. This small value faces two problems: i) if the bulk Lorentz factor Γ is larger than 150 (that is a necessary condition to avoid strong γ - γ opacity, see below), a small γ_m translates into a small efficiency of the electron acceleration, with $\epsilon_e < 0.05$, ii) the synchrotron peak energy can be located at $E_{\text{peak}}^{\text{syn}} \sim 10 \text{ keV}$ only for $B \Gamma \gtrsim 10^5 \text{ G}$. Large B and small ϵ_e would make difficult to explain the presence of a strong SSC emission. These calculations show that γ - γ opacity likely plays a role in shaping and softening the observed spectra of the SSC spectrum^{30,87}.

For a gamma-ray photon with energy E_γ , the $\tau_{\gamma\gamma}$ opacity is:

$$\tau_{\gamma\gamma}(E_\gamma) = \sigma_{\gamma\gamma}(R/\Gamma) n_t(E_\gamma), \quad (3)$$

where $n_t = L_t / (4 \pi R^2 c \Gamma E_t)$ is the density of target photons in the comoving frame, L_t is the luminosity and $E_t = (m_e c^2)^2 \Gamma^2 / E_\gamma / (1 + z)^2$ is the energy of target photons in the observer frame. Target photons for photons with energy $E_\gamma = 0.2 - 1 \text{ TeV}$ and for $\Gamma \sim 120 - 150$ have energies in the range $4 - 30 \text{ keV}$. When $\gamma - \gamma$ absorption is relevant, the emission from pairs can give a non-negligible contribution to the radiative output.

To properly model all the physical processes that are shaping the broadband radiation, we use a numerical code that solves the evolution of the electron distributions and derives the radiative

output taking into account the following processes: synchrotron and SSC losses, adiabatic losses, $\gamma - \gamma$ absorption, emission from pairs, and synchrotron self-absorption^{88–91}. We find that for the parameters assumed in the proposed modeling (see below), the contribution from pairs to the emission is negligible.

The MAGIC photon index (Extended Data Table 1) and its evolution with time constrain the SSC peak energy to be at $\lesssim 1$ TeV at the beginning of observations (Extended Data Table 1). In general the internal opacity decreases with time and KN effects become less relevant. A possible softening of the spectrum with time, as the one suggested by the observations, requires that the spectral peak decreases with time and moves below the MAGIC energy range. In the slow cooling regime, the SSC peak evolves to higher frequencies for a wind-like medium and decreases very slowly ($\nu_{\text{peak}}^{\text{SSC}} \propto t^{-1/4}$) for a constant-density medium (both in KN and Thomson regimes). In fast cooling regime the evolution is faster ($\nu_{\text{peak}}^{\text{SSC}} \propto t^{-1/2} - t^{-9/4}$ depending on medium and regime).

We model the **multi-band** observations considering both $s = 0$ and $s = 2$. The results are shown in Fig. 3, Extended Data Figs. 6 and 7 where model curves are overlaid to observations. The model curves shown in these figures have been derived using the following parameters. The model in Fig. 3 and in 7 (solid and dashed curves) we have used $s = 0$, $\epsilon_e = 0.07$, $\epsilon_B = 8 \times 10^{-5}$, $p = 2.6$, $n_0 = 0.5$, and $E_k = 8 \times 10^{53}$ erg. For the dotted curves in Extended Data Fig. 7 and the SEDs in Extended Data Figs. 6 we have used $s = 2$, $\epsilon_e = 0.6$, $\epsilon_B = 10^{-4}$, $p = 2.4$, $A_\star = 0.1$, and $E_k = 4 \times 10^{53}$ erg.

Using the constraints on the afterglow onset time ($t_{\text{peak}}^{\text{aft}} \sim 5 - 10$ s from the smooth compo-

693 nent detected during the prompt emission) the initial bulk Lorentz factor is constrained to assume
 694 values $\Gamma_0 \sim 300$ and $\Gamma_0 \sim 700$ for $s = 2$ and $s = 0$, respectively.

695 Consistently with **the** qualitative description above, we find that late time optical observa-
 696 tions can indeed be explained with ν_m crossing the band (see the SED modeling in Extended Data
 697 Fig. 6 and dotted curves in Extended Data Fig. 7). However a large ν_m is required in this case
 698 and consequently also the peak of the SSC component would be large and lie above the MAGIC
 699 energy range. The resulting MAGIC light curve (green dotted curve in Extended Data Fig. 7) does
 700 not agree with observations. Relaxing the requirement on ν_m , the TeV spectra (Fig. 3) and light
 701 curve (green solid curve in Extended Data Fig. 7) can be explained. As noted before, a wind-like
 702 medium can explain the steepening of the X-ray light curve at 8×10^4 s, while in a homogeneous
 703 medium no steepening is expected (blue dotted and solid lines in Extended Data Fig. 7). We find
 704 that the GeV flux detected by LAT at late time ($t \sim 10^4$ s) is dominated by the SSC component
 705 (dashed line in Extended Data Fig. 7).

- 706
- 708 1. Mészáros, P. Theories of Gamma-Ray Bursts. *ARA&A* **40**, 137–169 (2002).
 - 709 2. Piran, T. The physics of gamma-ray bursts. *Reviews of Modern Physics* **76**, 1143–1210 (2004).
 - 710 3. van Paradijs, J., Kouveliotou, C. & Wijers, R. A. M. J. Gamma-Ray Burst Afterglows.
 711 *ARA&A* **38**, 379–425 (2000).
 - 712 4. Gehrels, N., Ramirez-Ruiz, E. & Fox, D. B. Gamma-Ray Bursts in the Swift Era. *ARA&A*

- 713 **47**, 567–617 (2009).
- 714 5. Gehrels, N. & Mészáros, P. Gamma-Ray Bursts. *Science* **337**, 932 (2012).
- 715 6. Kumar, P. & Zhang, B. The physics of gamma-ray bursts & relativistic jets. *Phys. Rep.* **561**,
716 1–109 (2015).
- 717 7. Sari, R., Piran, T. & Narayan, R. Spectra and Light Curves of Gamma-Ray Burst Afterglows.
718 *ApJ* **497**, L17–L20 (1998).
- 719 8. Granot, J. & Sari, R. The Shape of Spectral Breaks in Gamma-Ray Burst Afterglows. *ApJ*
720 **568**, 820–829 (2002).
- 721 9. Meszaros, P. & Rees, M. J. Delayed GEV Emission from Cosmological Gamma-Ray Bursts -
722 Impact of a Relativistic Wind on External Matter. *MNRAS* **269**, L41 (1994).
- 723 10. MAGIC-Collaboration. Teraelectronvolt emission from a gamma-ray burst. *Nature* (2019).
- 724 11. Nava, L. High-energy emission from gamma-ray bursts. *International Journal of Modern*
725 *Physics D* **27**, 1842003 (2018).
- 726 12. Mirzoyan, R. First time detection of a GRB at sub-TeV energies; MAGIC detects the GRB
727 190114C. *The Astronomer’s Telegram* **12390** (2019).
- 728 13. Ajello, M. *et al.* Fermi and Swift Observations of GRB 190114C: Tracing the Evolution of
729 High-Energy Emission from Prompt to Afterglow. *arXiv e-prints* arXiv:1909.10605 (2019).
- 730 14. Ravasio, M. E. *et al.* GRB 190114C: from prompt to afterglow? *A&A* **626**, A12 (2019).

- 731 15. Laskar, T. *et al.* ALMA Detection of a Linearly Polarized Reverse Shock in GRB 190114C.
732 *ApJ* **878**, L26 (2019).
- 733 16. Vietri, M. GeV Photons from Ultrahigh Energy Cosmic Rays Accelerated in Gamma Ray
734 Bursts. *Physical Review Letters* **78**, 4328–4331 (1997).
- 735 17. Zhang, B. & Mészáros, P. High-Energy Spectral Components in Gamma-Ray Burst After-
736 glows. *ApJ* **559**, 110–122 (2001).
- 737 18. Razzaque, S. A Leptonic-Hadronic Model for the Afterglow of Gamma-ray Burst 090510.
738 *ApJ* **724**, L109–L112 (2010).
- 739 19. Sari, R. & Esin, A. A. On the Synchrotron Self-Compton Emission from Relativistic Shocks
740 and Its Implications for Gamma-Ray Burst Afterglows. *ApJ* **548**, 787–799 (2001).
- 741 20. Mészáros, P., Razzaque, S. & Zhang, B. GeV-TeV emission from γ -ray bursts. *New A Rev.*
742 **48**, 445–451 (2004).
- 743 21. Lemoine, M. The synchrotron self-Compton spectrum of relativistic blast waves at large Y .
744 *MNRAS* **453**, 3772–3784 (2015).
- 745 22. Fan, Y.-Z. & Piran, T. High-energy γ -ray emission from gamma-ray bursts — before GLAST.
746 *Frontiers of Physics in China* **3**, 306–330 (2008).
- 747 23. Galli, A. & Piro, L. Prospects for detection of very high-energy emission from GRB in the
748 context of the external shock model. *A&A* **489**, 1073–1077 (2008).

- 749 24. Nakar, E., Ando, S. & Sari, R. Klein-Nishina Effects on Optically Thin Synchrotron and
750 Synchrotron Self-Compton Spectrum. *ApJ* **703**, 675–691 (2009).
- 751 25. Xue, R. R. *et al.* Very High Energy γ -Ray Afterglow Emission of Nearby Gamma-Ray Bursts.
752 *ApJ* **703**, 60–67 (2009).
- 753 26. Piran, T. & Nakar, E. On the External Shock Synchrotron Model for Gamma-ray Bursts’ GeV
754 Emission. *ApJ* **718**, L63–L67 (2010).
- 755 27. Tam, P.-H. T., Tang, Q.-W., Hou, S.-J., Liu, R.-Y. & Wang, X.-Y. Discovery of an Extra Hard
756 Spectral Component in the High-energy Afterglow Emission of GRB 130427A. *ApJ* **771**, L13
757 (2013).
- 758 28. Liu, R.-Y., Wang, X.-Y. & Wu, X.-F. Interpretation of the Unprecedentedly Long-lived High-
759 energy Emission of GRB 130427A. *ApJ* **773**, L20 (2013).
- 760 29. Ackermann, M. *et al.* Fermi-LAT Observations of the Gamma-Ray Burst GRB 130427A.
761 *Science* **343**, 42–47 (2014).
- 762 30. Wang, X.-Y., Liu, R.-Y., Zhang, H.-M., Xi, S.-Q. & Zhang, B. Synchrotron self-Compton
763 emission from afterglow shocks as the origin of the sub-TeV emission in GRB 180720B and
764 GRB 190114C. *arXiv e-prints* arXiv:1905.11312 (2019).
- 765 31. Hamburg, R. GRB 190114C: Fermi GBM detection. *GRB Coordinates Network* **23707** (2019).
- 766 32. Kocevski, D. *et al.* GRB 190114C: Fermi-LAT detection. *GRB Coordinates Network* **23709**
767 (2019).

- 768 33. Gropp, J. D. GRB 190114C: Swift detection of a very bright burst with a bright optical
769 counterpart. *GRB Coordinates Network* **23688** (2019).
- 770 34. Ursi, A. *et al.* GRB 190114C: AGILE/MCAL detection. *GRB Coordinates Network* **23712**
771 (2019).
- 772 35. Frederiks, D. *et al.* Konus-Wind observation of GRB 190114C. *GRB Coordinates Network*
773 **23737** (2019).
- 774 36. Minaev, P. & Pozanenko, A. GRB 190114C: SPI-ACS/INTEGRAL extended emission detec-
775 tion. *GRB Coordinates Network* **23714** (2019).
- 776 37. Xiao, S. *et al.* GRB 190114C:Insight-HXMT/HE detection. *GRB Coordinates Network* **23716**
777 (2019).
- 778 38. Tavani, M. *et al.* The AGILE Mission. *Astron. Astrophys.* **502**, 995–1013 (2009).
- 779 39. Goldstein, A. *et al.* The Fermi GBM Gamma-Ray Burst Spectral Catalog: The First Two
780 Years. *ApJS* **199**, 19 (2012).
- 781 40. Meegan, C. *et al.* The Fermi Gamma-ray Burst Monitor. *ApJ* **702**, 791–804 (2009).
- 782 41. Barthelmy, S. D. *et al.* The Burst Alert Telescope (BAT) on the SWIFT Midex Mission.
783 *Space Sci. Rev.* **120**, 143–164 (2005).
- 784 42. Atwood, A. A., W. B. Abdo *et al.* The Large Area Telescope on the Fermi Gamma-Ray Space
785 Telescope Mission. *ApJ* **697**, 1071–1102 (2009).

- 786 43. Kocevski, D. *et al.* GRB 190114C: Fermi-LAT detection. *GRB Coordinates Network* **23709**
787 (2019).
- 788 44. Aleksić, J. *et al.* The major upgrade of the MAGIC telescopes, Part II: A performance study
789 using observations of the Crab Nebula. *Astroparticle Physics* **72**, 76–94 (2016).
- 790 45. Ahnen, M. L. *et al.* Performance of the MAGIC telescopes under moonlight. *Astroparticle*
791 *Physics* **94**, 29–41 (2017).
- 792 46. Domínguez, A. *et al.* Extragalactic background light inferred from AEGIS galaxy-SED-type
793 fractions. *MNRAS* **410**, 2556–2578 (2011).
- 794 47. Franceschini, A., Rodighiero, G. & Vaccari, M. Extragalactic optical-infrared background ra-
795 diation, its time evolution and the cosmic photon-photon opacity. *A&A* **487**, 837–852 (2008).
- 796 48. Finke, J. D., Razzaque, S. & Dermer, C. D. Modeling the Extragalactic Background Light
797 from Stars and Dust. *ApJ* **712**, 238–249 (2010).
- 798 49. Gilmore, R. C., Somerville, R. S., Primack, J. R. & Domínguez, A. Semi-analytic modelling
799 of the extragalactic background light and consequences for extragalactic gamma-ray spectra.
800 *MNRAS* **422**, 3189–3207 (2012).
- 801 50. UK *Swift* Science Data Centre. GRB 190114C *Swift*/XRT Light Curve. [https://www.](https://www.swift.ac.uk/xrt_curves/00883832/)
802 [swift.ac.uk/xrt_curves/00883832/](https://www.swift.ac.uk/xrt_curves/00883832/).
- 803 51. Evans, P. A. *et al.* Methods and results of an automatic analysis of a complete sample of
804 *Swift*-XRT observations of GRBs. *MNRAS* **397**, 1177–1201 (2009).

- 805 52. Greiner, J. *et al.* GROND—a 7-Channel Imager. *Publications of the Astronomical Society of*
806 *the Pacific* **120**, 405 (2008).
- 807 53. Tody, D. IRAF in the Nineties. In Hanisch, R. J., Brissenden, R. J. V. & Barnes, J. (eds.)
808 *Astronomical Data Analysis Software and Systems II*, vol. 52 of *Astronomical Society of the*
809 *Pacific Conference Series*, 173 (1993).
- 810 54. Krühler, T. *et al.* The 2175 Å Dust Feature in a Gamma-Ray Burst Afterglow at Redshift 2.45.
811 *ApJ* **685**, 376–383 (2008).
- 812 55. Bolmer, J. *et al.* Dust reddening and extinction curves toward gamma-ray bursts at $z > 4$.
813 *A&A* **609**, A62 (2018).
- 814 56. Castro-Tirado, A. J. *et al.* A very sensitive all-sky CCD camera for continuous recording of
815 the night sky. In Proc. SPIE, vol. 7019 of *Society of Photo-Optical Instrumentation Engineers*
816 *(SPIE) Conference Series*, 70191V (2008).
- 817 57. Cepa, J. *et al.* OSIRIS tunable imager and spectrograph. In Iye, M. & Moorwood, A. F. (eds.)
818 *Optical and IR Telescope Instrumentation and Detectors*, vol. 4008 of Proc. SPIE, 623–631
819 (2000).
- 820 58. Castro-Tirado, A. GRB 190114C: refined redshift by the 10.4m GTC. *GRB Coordinates*
821 *Network* **23708** (2019).
- 822 59. de Ugarte Postigo, A. *et al.* The distribution of equivalent widths in long GRB afterglow
823 spectra. *A&A* **548**, A11 (2012).

- 824 60. Steele, I. A. *et al.* The Liverpool Telescope: performance and first results. In Oschmann, J. M.,
825 Jr. (ed.) *Ground-based Telescopes*, vol. 5489 of Proc. SPIE, 679–692 (2004).
- 826 61. Chambers, K. C. *et al.* The Pan-STARRS1 Surveys. *arXiv e-prints* (2016).
- 827 62. Tarenghi, M. & Wilson, R. N. The ESO NTT (New Technology Telescope): The first active
828 optics telescope. In Roddier, F. J. (ed.) *Active telescope systems*, vol. 1114 of *Society of Photo-*
829 *Optical Instrumentation Engineers (SPIE) Conference Series*, 302–313 (1989).
- 830 63. Smartt, S. J. *et al.* PESSTO: survey description and products from the first data release by the
831 Public ESO Spectroscopic Survey of Transient Objects. *A&A* **579**, A40 (2015).
- 832 64. Covino, S. *et al.* REM: a fully robotic telescope for GRB observations. In Moorwood, A.
833 F. M. & Iye, M. (eds.) *Ground-based Instrumentation for Astronomy*, vol. 5492 of *Society of*
834 *Photo-Optical Instrumentation Engineers (SPIE) Conference Series*, 1613–1622 (2004).
- 835 65. Roming, P. W. A. *et al.* The Swift Ultra-Violet/Optical Telescope. *Space Sci. Rev.* **120**, 95–142
836 (2005).
- 837 66. Siegel, M. H. & Gropp, J. D. GRB 190114C: Swift/UVOT Detection. *GRB Coordinates*
838 *Network* **23725** (2019).
- 839 67. Poole, T. S. *et al.* Photometric calibration of the Swift ultraviolet/optical telescope. *MNRAS*
840 **383**, 627–645 (2008).
- 841 68. Breeveld, A. A. *et al.* An Updated Ultraviolet Calibration for the Swift/UVOT. In *American*
842 *Institute of Physics Conference Series*, vol. 1358, 373–376 (2011).

- 843 69. Kuin, N. P. M. *et al.* Calibration of the Swift-UVOT ultraviolet and visible grisms. MNRAS
844 **449**, 2514–2538 (2015).
- 845 70. Arnouts, S. *et al.* Measuring and modelling the redshift evolution of clustering: the Hubble
846 Deep Field North. MNRAS **310**, 540–556 (1999).
- 847 71. Ilbert, O. *et al.* Accurate photometric redshifts for the CFHT legacy survey calibrated using
848 the VIMOS VLT deep survey. A&A **457**, 841–856 (2006).
- 849 72. Covino, S. *et al.* Dust extinctions for an unbiased sample of gamma-ray burst afterglows.
850 MNRAS **432**, 1231–1244 (2013).
- 851 73. Schlafly, E. F. & Finkbeiner, D. P. Measuring Reddening with Sloan Digital Sky Survey Stellar
852 Spectra and Recalibrating SFD. ApJ **737**, 103 (2011).
- 853 74. McMullin, J. P., Waters, B., Schiebel, D., Young, W. & Golap, K. CASA Architecture and
854 Applications. In Shaw, R. A., Hill, F. & Bell, D. J. (eds.) *Astronomical Data Analysis Soft-*
855 *ware and Systems XVI*, vol. 376 of *Astronomical Society of the Pacific Conference Series*, 127
856 (2007).
- 857 75. Wilson, W. E. *et al.* The Australia Telescope Compact Array Broad-band Backend: description
858 and first results. MNRAS **416**, 832–856 (2011).
- 859 76. Sault, R. J., Teuben, P. J. & Wright, M. C. H. A Retrospective View of MIRIAD. In Shaw,
860 R. A., Payne, H. E. & Hayes, J. J. E. (eds.) *Astronomical Data Analysis Software and Systems*
861 *IV*, vol. 77 of *Astronomical Society of the Pacific Conference Series*, 433 (1995).

- 862 77. Swarup, G. *et al.* The Giant Metre-Wave Radio Telescope. *Current Science*, Vol. 60,
863 *NO.2/JAN25*, P. 95, 1991 **60**, 95 (1991).
- 864 78. Cherukuri, S. V. *et al.* GRB 190114C: GMRT detection at 1.26GHz. *GRB Coordinates Net-*
865 *work* **23762** (2019).
- 866 79. Tremou, L. *et al.* GRB 190114C: MeerKAT radio observation. *GRB Coordinates Network*
867 **23760** (2019).
- 868 80. Camilo, F. *et al.* Revival of the Magnetar PSR J1622-4950: Observations with MeerKAT,
869 Parkes, XMM-Newton, Swift, Chandra, and NuSTAR. *ApJ* **856**, 180 (2018).
- 870 81. Jonas, J. & MeerKAT Team. The MeerKAT Radio Telescope. In *Proceedings of MeerKAT*
871 *Science: On the Pathway to the SKA*. 25-27 May, 1 (2016).
- 872 82. Fender, R. *et al.* ThunderKAT: The MeerKAT Large Survey Project for Image-Plane Radio
873 Transients. *arXiv e-prints* arXiv:1711.04132 (2017).
- 874 83. Mohan, N. & Rafferty, D. PyBDSF: Python Blob Detection and Source Finder (2015).
- 875 84. Holland, W. S. *et al.* SCUBA-2: the 10 000 pixel bolometer camera on the James Clerk
876 Maxwell Telescope. *MNRAS* **430**, 2513–2533 (2013).
- 877 85. Bošnjak, Ž., Daigne, F. & Dubus, G. Prompt high-energy emission from gamma-ray bursts in
878 the internal shock model. *A&A* **498**, 677–703 (2009).
- 879 86. Panaitescu, A. & Kumar, P. Analytic Light Curves of Gamma-Ray Burst Afterglows: Homo-
880 geneous versus Wind External Media. *ApJ* **543**, 66–76 (2000).

- 881 87. Derishev, E. & Piran, T. The Physical Conditions of the Afterglow Implied by MAGIC's
882 Sub-TeV Observations of GRB 190114C. *ApJ* **880**, L27 (2019).
- 883 88. Mastichiadis, A. & Kirk, J. G. Self-consistent particle acceleration in active galactic nuclei.
884 *A&A* **295**, 613 (1995).
- 885 89. Vurm, I. & Poutanen, J. Time-Dependent Modeling of Radiative Processes in Hot Magnetized
886 Plasmas. *ApJ* **698**, 293–316 (2009).
- 887 90. Petropoulou, M. & Mastichiadis, A. On the multiwavelength emission from gamma ray burst
888 afterglows. *A&A* **507**, 599–610 (2009).
- 889 91. Pennanen, T., Vurm, I. & Poutanen, J. Simulations of gamma-ray burst afterglows with a
890 relativistic kinetic code. *A&A* **564**, A77 (2014).

891 **Author Information** The authors declare no competing interests. Correspondence and requests for mate-
892 rials should be addressed to Razmik Mirzoyan (email: razmik.mirzoyan@mpp.mpg.de) or MAGIC (email:
893 contact.magic@mpp.mpg.de).

894 **Acknowledgements** The MAGIC Collaboration would like to thank the Instituto de Astrofísica de Ca-
895 narias for the excellent working conditions at the Observatorio del Roque de los Muchachos in La Palma.
896 The financial support of the German BMBF and MPG, the Italian INFN and INAF, the Swiss National
897 Fund SNF, the ERDF under the Spanish MINECO (FPA2017-87859-P, FPA2017-85668-P, FPA2017-82729-
898 C6-2-R, FPA2017-82729-C6-6-R, FPA2017-82729-C6-5-R, AYA2015-71042-P, AYA2016-76012-C3-1-P,
899 ESP2017-87055-C2-2-P, FPA201790566REDC), the Indian Department of Atomic Energy, the Japanese

900 JSPS and MEXT, the Bulgarian Ministry of Education and Science, National RI Roadmap Project DO1-
 901 153/28.08.2018 and the Academy of Finland grant nr. 320045 is gratefully acknowledged. This work
 902 was also supported by the Spanish Centro de Excelencia “Severo Ochoa” SEV-2016-0588 and SEV-2015-
 903 0548, and Unidad de Excelencia “María de Maeztu” MDM-2014-0369, by the Croatian Science Foun-
 904 dation (HrZZ) Project IP-2016-06-9782 and the University of Rijeka Project 13.12.1.3.02, by the DFG
 905 Collaborative Research Centers SFB823/C4 and SFB876/C3, the Polish National Research Centre grant
 906 UMO-2016/22/M/ST9/00382 and by the Brazilian MCTIC, CNPq and FAPERJ. L. Nava acknowledges
 907 funding from the European Union’s Horizon 2020 Research and Innovation programme under the Marie
 908 Skłodowska-Curie grant agreement n. 664931. E. Moretti acknowledges funding from the European Union’s
 909 Horizon 2020 research and innovation programme under Marie Skłodowska-Curie grant agreement No
 910 665919. This paper makes use of the following ALMA data: ADS/JAO.ALMA#2018.A.00020.T,
 911 ADS/JAO.ALMA#2018.1.01410.T. ALMA is a partnership of ESO (representing its member states), NSF
 912 (USA) and NINS (Japan), together with NRC (Canada), MOST and ASIAA (Taiwan), and KASI (Repub-
 913 lic of Korea), in cooperation with the Republic of Chile. The Joint ALMA Observatory is operated by
 914 ESO, AUI/NRAO and NAOJ. CT, AdUP, and DAK acknowledge support from the Spanish research project
 915 AYA2017-89384-P. C. Thoene and A. de Ugarte Postigo acknowledge support from funding associated to
 916 Ramón y Cajal fellowships (RyC-2012-09984 and RyC-2012-09975). D. A. Kann acknowledges support
 917 from funding associated to Juan de la Cierva Incorporación fellowships (IJCI-2015-26153). The James Clerk
 918 Maxwell Telescope is operated by the East Asian Observatory on behalf of The National Astronomical Ob-
 919 servatory of Japan; Academia Sinica Institute of Astronomy and Astrophysics; the Korea Astronomy and
 920 Space Science Institute; Center for Astronomical Mega-Science (as well as the National Key R&D Program
 921 of China with No. 2017YFA0402700). Additional funding support is provided by the Science and Tech-
 922 nology Facilities Council of the United Kingdom and participating universities in the United Kingdom and

923 Canada. The JCMT data reported here were obtained under project M18BP040 (P.I. D. Perley). We thank
924 Mark Rawlings, Kevin Silva, Sheona Urquart, and the JCMT staff for the prompt support of these observa-
925 tions. The Liverpool Telescope, located on the island of La Palma in the Spanish Observatorio del Roque de
926 los Muchachos of the Instituto de Astrofísica de Canarias, is operated by Liverpool John Moores University
927 with financial support from the UK Science and Technology Facilities Council. The Australia Telescope
928 Compact Array is part of the Australia Telescope National Facility which is funded by the Australian Gov-
929 ernment for operation as a National Facility managed by CSIRO. GEA is the recipient of an Australian
930 Research Council Discovery Early Career Researcher Award (project number DE180100346) and JCAM-J
931 is the recipient of Australian Research Council Future Fellowship (project number FT140101082) funded by
932 the Australian Government. Support for the German contribution to GBM was provided by the Bundesmin-
933 isterium für Bildung und Forschung (BMBF) via the Deutsches Zentrum für Luft und Raumfahrt (DLR)
934 under grant number 50 QV 0301. The UAH coauthors gratefully acknowledge NASA funding from coop-
935 erative agreement NNM11AA01A. C.A.W.H., and C.M.H. gratefully acknowledge NASA funding through
936 the *Fermi*-GBM project.

937 The *Fermi* LAT Collaboration acknowledges generous ongoing support from a number of agencies and in-
938 stitutes that have supported both the development and the operation of the LAT as well as scientific data
939 analysis. These include the National Aeronautics and Space Administration and the Department of Energy
940 in the United States, the Commissariat à l’Énergie Atomique and the Centre National de la Recherche Sci-
941 entifique / Institut National de Physique Nucléaire et de Physique des Particules in France, the Agenzia
942 Spaziale Italiana and the Istituto Nazionale di Fisica Nucleare in Italy, the Ministry of Education, Cul-
943 ture, Sports, Science and Technology (MEXT), High Energy Accelerator Research Organization (KEK) and
944 Japan Aerospace Exploration Agency (JAXA) in Japan, and the K. A. Wallenberg Foundation, the Swedish
945 Research Council and the Swedish National Space Board in Sweden.

946 Additional support for science analysis during the operations phase is gratefully acknowledged from the
947 Istituto Nazionale di Astrofisica in Italy and the Centre National d'Études Spatiales in France. This work
948 performed in part under DOE Contract DE-AC02-76SF00515.

949 Part of the funding for GROND (both hardware as well as personnel) was generously granted from the
950 Leibniz-Prize to Prof. G. Hasinger (DFG grant HA 1850/28-1). Swift data were retrieved from the Swift
951 archive at HEASARC/NASA-GSFC, and from the UK Swift Science Data Centre. Support for Swift in the
952 UK is provided by the UK Space Agency

953 This work is based on observations obtained with XMM-Newton, an ESA science mission with instruments
954 and contributions directly funded by ESA Member States and NASA.

955 This work is partially based on observations collected at the European Organisation for Astronomical Re-
956 search in the Southern Hemisphere under ESO programme 199.D-0143. The work is partly based on ob-
957 servations made with the Gran Telescopio Canarias (GTC), installed in the Spanish Observatorio del Roque
958 de los Muchachos of the Instituto de Astrofísica de Canarias, in the island of La Palma. This work is par-
959 tially based on observations made with the Nordic Optical Telescope (programme 58-502), operated by the
960 Nordic Optical Telescope Scientific Association at the Observatorio del Roque de los Muchachos, La Palma,
961 Spain, of the Instituto de Astrofísica de Canarias. This work is partially based on observations collected at
962 the European Organisation for Astronomical Research in the Southern Hemisphere under ESO programme
963 102.D-0662. This work is partially based on observations collected through the ESO programme 199.D-
964 0143 ePESSTO. M. Gromadzki is supported by the Polish NCN MAESTRO grant 2014/14/A/ST9/00121.
965 M. Nicholl is supported by a Royal Astronomical Society Research Fellowship M. G. Bernardini, S. Cam-
966 pana, A. Melandri and P. D'Avanzo acknowledge ASI grant I/004/11/3. S. Campana thanks for support the
967 implementing agreement ASI-INAF n.2017-14-H.0. S. J. Smartt acknowledges funding from STFC Grant

Ref: ST/P000312/1. NPMK acknowledges support by the UK Space Agency under grant ST/P002323/1 and the UK Science and Technology Facilities Council under grant ST/N00811/1. L. Piro, S. Lotti acknowledge partial support from the agreement ASI-INAF n.2017-14-H.0. VAF acknowledges RFBR 18-29-21030 for support. AJCT acknowledges support from the Junta de Andalucía (Project P07-TIC-03094) and support from the Spanish Ministry Projects AYA2012-39727-C03-01 and 2015-71718R. KM acknowledges the support from Department of Science and Technology (DST), Govt. of India and Indo-US Science and Technology Forum (IUSSTF) for the WISTEMM fellowship and Dept. of Physics, UC Davis where a part of this work was carried out. M.J.M. acknowledges the support of the National Science Centre, Poland through the grant 2018/30/E/ST9/00208. VJ and RL acknowledges support from the grant EMR/2016/007127 from Dept. of Science and Technology, India. K. Maguire acknowledges support from H2020 through an ERC Starting Grant (758638). L. Izzo would like to acknowledge Massimo Della Valle for invaluable support in the operation of the telescope.

Author Contributions The MAGIC telescope system was designed and constructed by the MAGIC Collaboration. Operation, data processing, calibration, Monte Carlo simulations of the detector, and of theoretical models, and data analyses were performed by the members of the MAGIC Collaboration, who also discussed and approved the scientific results. L. Nava coordinated the gathering of the data, developed the theoretical interpretation, and wrote the main section and the section on Afterglow Modeling. E. Moretti coordinated the analysis of the MAGIC data, wrote the relevant sections, and, together with F. Longo, coordinated the collaboration with the Fermi team. D. Miceli, Y. Suda and S. Fukami performed the analysis of the MAGIC data. S. Covino provided support with the analysis of the optical data and the writing of the corresponding sections. Z. Bosnjak performed calculations for the contribution from prompt emission to TeV radiation and wrote the corresponding section. A. Stamerra, D. Paneque and S. Inoue contributed in

990 structuring and editing the paper. A. Berti contributed to editing and finalising the manuscript. R. Mirzoyan
 991 coordinated and supervised the paper. All MAGIC collaborators contributed to the editing and comments to
 992 the final version of the manuscript.

993 S. Campana and M. G. Bernardini extracted the spectra and performed the spectral analysis of *Swift*/BAT
 994 and *Swift*/XRT data. N. P. M. Kuin derived the photometry for the *Swift*/UVOT event mode data, and the uv
 995 grism exposure. M. H. Siegel derived the image mode Swift UVOT photometry. A. de Ugarte Postigo was
 996 principal investigator of ALMA program 2018.1A.00020.T, triggered these observations and performed
 997 photometry. S. Martin reduced the ALMA Band 6 data. C. C. Thöne, S. Schulze, D. A. Kann, and M.
 998 Michałowski participated in the ALMA DDT proposal preparation, observations, and scientific analysis of
 999 the data. D. A. Perley was principal investigator of ALMA program 2018.1.01410.T and triggered these
 1000 observations, and was also principal investigator of the LT programme and the JCMT programme. A. M.
 1001 Cockeram analyzed the ALMA Band 3 and LT data, and wrote the LT text. S. Schulze contributed to the
 1002 development of the ALMA Band 3 observing programme. I. A. Smith triggered the JCMT programme,
 1003 analyzed the data, and wrote the associated text. N. R. Tanvir contributed to the development of the JCMT
 1004 programme. D. A. Kann and C. C. Thöne triggered and coordinated the X-shooter observations. D. A. Kann
 1005 independently checked the optical light curve analysis. K. Misra was the principal investigator of the GMRT
 1006 programme 35_018. S. V. Cherukuri and V. Jaiswal analyzed the data. L. Resmi contributed to the observa-
 1007 tion plan and data analysis. E.T., I.H. and R.D. have performed the MeerKAT data analysis. G. Anderson,
 1008 A. Moin, S. Schulze and E. Troja were principal investigator of ATCA program CX424. G. Anderson, M.
 1009 Wieringa and J. Stevens carried out the observations. G. Anderson, G. Bernardi, S. Klose, M. Marongiu, A.
 1010 Moin, R. Ricci and M. Wieringa analysed these data. M. Bell, J. Miller-Jones and L. Piro participated to the
 1011 ATCA proposal preparation and scientific analysis of the data. The ePESSTO project was delivered by the
 1012 following who have contributed to managing, executing, reducing, analysing ESO/NTT data and provided

1013 comments to the manuscript: J. P. Anderson, N. Castro Segura, P. D’Avanzo, M. Gromadzki, C. Inserra,
1014 E. Kankare, K. Maguire, M. Nicholl, F. Ragosta, S. J. Smartt. A. Melandri and A. Rossi reduced and an-
1015 alyzed REM data and provided comments to the manuscript. J. Bolmer was responsible for observing the
1016 GRB with GROND as well as for the data reduction and calibration. J. Bolmer and J. Greiner contributed to
1017 the analysis of the data and writing of the text. E. Troja triggered the *NuSTAR* TOO observations performed
1018 under DDT program, L. Piro requested the XMM-Newton data carried out under DDT program and carried
1019 out the scientific analysis of XMM-Newton and *NuSTAR*. S. Lotti analyzed the *NuSTAR* data and wrote the
1020 associated text. A. Tiengo and G. Novara analysed the XMM-Newton data and wrote the associated text.
1021 AJCT led the observing BOOTES and GTC programs. AC, CJPP, EFG, IMC, SBP and XYL analyzed the
1022 BOOTES data whereas AFV, MDCG, RSR, YDH and VVS analyzed the GTC data and interpreted them
1023 accordingly. N. Tanvir created the X-shooter and AIFOSC figures. J. Fynbo, J. Japelj performed the analy-
1024 sis of X-shooter and AIFOSC spectra. D. Xu, P. Jakobsson contributed to NOT programme and triggering.
1025 D. Malesani performed photometric analysis of NOT data. E. Peretti contributed to developing the code for
1026 modeling of afterglow radiation. L. Izzo triggered and analysed the OASDG data, while A. Di Dato and A.
1027 Noschese executed the observations at the telescope.

1028 **Data Availability Statement** Data are available from the corresponding authors upon request.

1029 **Code Availability Statement** Proprietary data reconstruction codes were generated at the MAGIC tele-
1030 scopes large-scale facility. Information supporting the findings of this study are available from the corre-
1031 sponding authors upon request.